Atmospheric Environment 368 (2026) 121767

Contents lists available at ScienceDirect

Atmospheric Environment

journal homepage: www.elsevier.com/locate/atmosenv

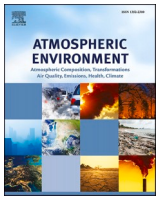

Validation of satellite formaldehyde products constrained by aircraft observations over the United States during fire seasons

Shuai Sun [a,b,c], Yuzhong Zhang [b,c,*], Song Liu [d], Lei Shu [e], Isabelle De Smedt [f], Lu Hu [g], Wade Permar [g], Dirk Richter [h], Alan Fried [h], Lei Zhu [d,i,j,**]

[a] College of Environmental and Resource Sciences, Zhejiang University, Hangzhou, Zhejiang, China
[b] Key Laboratory of Coastal Environment and Resources of Zhejiang Province, School of Engineering, Westlake University, Hangzhou, Zhejiang, China
[c] Institute of Advanced Technology, Westlake Institute for Advanced Study, Hangzhou, Zhejiang, China
[d] School of Environmental Science and Engineering, Southern University of Science and Technology, Shenzhen, Guangdong, China
[e] School of Geographical Sciences, Fujian Normal University, Fuzhou, Fujian, China
[f] Royal Belgian Institute for Space Aeronomy (BIRA-IASB), Brussels, Belgium
[g] Department of Chemistry and Biochemistry, University of Montana, Missoula, MT, USA
[h] Institute of Arctic and Alpine Research, University of Colorado, Boulder, CO, USA
[i] Guangdong Provincial Observation and Research Station for Coastal Atmosphere and Climate of the Greater Bay Area, Shenzhen, Guangdong, China
[j] Shenzhen Key Laboratory of Precision Measurement and Early Warning Technology for Urban Environmental Health Risks, School of Environmental Science and Engineering, Southern University of Science and Technology, Shenzhen, China

HIGHLIGHTS

- An aircraft-constrained indirect approach offers a valuable reference for assessing satellite HCHO retrievals.
- Five satellite HCHO products show consistent low bias (11.0–56.7%) during fire seasons, with OMPS-SAO (N20) performing best.
- HCHO retrieval uncertainties during fires stem from profile shape, slant column fitting, and aerosol/cloud scattering.

ABSTRACT

Satellite-derived formaldehyde (HCHO) column densities are commonly used to infer regional emissions of non-methane volatile organic compounds (NMVOCs). However, intercomparison and validation of HCHO retrievals from different satellite sensors remain scarce, especially under fire periods. Here, we use observations from FIREX-AQ (Fire Influence on Regional to Global Environments and Air Quality experiment) and WE-CAN (Western Wildfire Experiment for Cloud Chemistry, Aerosol and Nitrogen), two flight campaigns dedicated to investigating smoke plumes during active fire seasons, combined with simulations from the GEOS-Chem to intercompare and validate five HCHO products from four satellites (OMI, OMPS-NPP, OMPS-N20, and TROPOMI). Our analysis suggests that all satellite products consistently capture elevated HCHO signals over the southeastern US and California, but they tend to report lower column values compared to our aircraft-constrained model estimates, with differences ranging from 11.0 % to 56.7 %. Our results imply that while vertical profile shape (reflected in the air mass factor, AMF) plays a role, errors in the slant column retrieval and the treatment of aerosol and cloud scattering effects may be key sources of uncertainty in the satellite HCHO products during fire events. Therefore, future retrieval improvements should prioritize better aerosol and slant column accuracy to reduce biases.

1. Introduction

Formaldehyde (HCHO) is a prevalent trace gas in the troposphere, primarily generated through the atmospheric oxidation of a wide array of volatile organic compounds (VOCs), with the oxidation of methane constituting the dominant source that establishes the baseline background concentration. With an atmospheric lifetime of a few hours against photolysis and oxidation, HCHO, especially its local enhancement, is related to the underlying short-lived non-methane VOC (NMVOC) emissions from biogenic (Ferreira et al., 2010; Fu et al., 2007; Palmer et al., 2003), anthropogenic (Bauwens et al., 2022; Lieschke et al., 2019; Martin et al., 2004), and biomass burning sources (Baek

* Corresponding author. Key Laboratory of Coastal Environment and Resources of Zhejiang Province, School of Engineering, Westlake University, Hangzhou, Zhejiang, China.
** Corresponding author. School of Environmental Science and Engineering, Southern University of Science and Technology, Shenzhen, Guangdong, China.
E-mail addresses: zhangyuzhong@westlake.edu.cn (Y. Zhang), zhul3@sustech.edu.cn (L. Zhu).

https://doi.org/10.1016/j.atmosenv.2025.121767
Received 23 October 2025; Received in revised form 9 December 2025; Accepted 30 December 2025
Available online 7 January 2026
1352-2310/© 2026 Elsevier Ltd. All rights are reserved, including those for text and data mining, AI training, and similar technologies.

et al., 2014; De Smedt et al., 2010; Kim et al., 2011; Su et al., 2019; Zhang et al., 2019). As such, satellite HCHO vertical column density (VCD; in a unit of molecules cm^{-2}) has been widely employed as an indicator of localized NMVOC emissions (Barkley et al., 2013; De Smedt et al., 2021; Fan et al., 2021; Levelt et al., 2022; Liu et al., 2018; Millet et al., 2006; Sun et al., 2021). However, validation of satellite HCHO data remains limited, particularly during fire seasons when substantial quantities of NMVOCs and aerosols are emitted into the atmosphere and transported downwind (Akagi et al., 2012; Liang et al., 2022; Yokelson et al., 2007). This study validates and intercompares five satellite HCHO products from four satellites over the United States (US) during fire seasons using *in situ* observations from the Fire Influence on Regional to Global Environments and Air Quality experiment (FIREX-AQ; Warneke et al., 2022) and the Western Wildfire Experiment for Cloud Chemistry, Aerosol and Nitrogen (WE-CAN; Lindaas et al., 2021; Palm et al., 2021; Permar et al., 2021) flight campaigns.

Tropospheric HCHO VCDs were first retrieved from the Global Ozone Monitoring Experiment (GOME) (1996–2003) (Chance et al., 2000; Martin et al., 2004; Palmer et al., 2003), followed by the SCanning Imaging Absorption SpectroMeter for Atmospheric CHartographY (SCIAMACHY) (2003–2012) (Barkley et al., 2013; De Smedt et al., 2008; Wittrock et al., 2006). Currently, satellite HCHO retrievals are made available from the Ozone Monitoring Instrument (OMI) (2004–) (González Abad et al., 2015; Jung et al., 2019), GOME-2A (2006–2021) (De Smedt et al., 2015; Hewson et al., 2013), Ozone Mapping and Profiler Suite (OMPS) on Suomi NPP (2011–) (González Abad et al., 2016; Li et al., 2015; Su et al., 2019) and on NOAA-20 (2017−) (Nowlan et al., 2023), GOME-2B (2012–) (De Smedt et al., 2012, 2015; Hassinen et al., 2016), and TROPOspheric Monitoring Instrument (TROPOMI) (2018–) (De Smedt et al., 2018; Su et al., 2020). In the era of the geostationary constellation, the Geostationary Environment Monitoring Spectrometer (GEMS) (2020–; Kim et al., 2020; Kwon et al., 2019), Tropospheric emissions: Monitoring of pollution (TEMPO) (2023; Zoogman et al., 2017), and Sentinel-4 (2023; Ingmann et al., 2012) will provide hourly HCHO observations during daylight hours across East Asia, North America, and Europe, respectively.

Retrieving HCHO from space generally involves two steps: (1) fitting the slant column density (SCD) within the 325–360 nm spectral window (Chance et al., 2000) (2) converting the resulted SCD to VCD with air mass factor (AMF). As for the SCD fitting, the uncertainty is mainly from instrument characteristics and slant column fitting procedure, such as measurement noise, HCHO cross-section error, and choice of fitting windows, whereas the uncertainty of AMF is mainly from its input parameters, including the surface albedos, *a priori* profiles, vertical profiles of clouds and aerosols as well as their amounts (Barkley et al., 2012; Jung et al., 2019; Lorente et al., 2017; Millet et al., 2006; Palmer et al., 2001).

Biomass burning emits considerable quantities of trace gases and aerosols, significantly affecting air quality, public health, and climate dynamics (Andreae and Merlet, 2001; Kunzli et al., 2006; Liao et al., 2019; Xu et al., 2022; Zhang et al., 2020). As a highly emitted NMVOC from wildfires (Gilman et al., 2015; Liao et al., 2021), HCHO, including primary emission and secondary formation, has been observed in an elevated manner in the Amazon (Kesselmeier et al., 2002), Canada (Alvarado et al., 2020; Gonzi et al., 2011; Wolfe et al., 2022), European Russia (Sitnov, S. A. and Mokhov, 2017), Western US (Baker et al., 2018; Liao et al., 2021; Lill et al., 2022; Permar et al., 2023), and US Alaska (Zhao et al., 2022). Similarly, satellite observations also show high HCHO VCDs consistent with the distribution of wildfires (Fu et al., 2018; Marais et al., 2012; Marbach et al., 2008).

Emissions from intense biomass burning events can penetrate into the free troposphere, and in some cases, extend into the upper troposphere (Dahlkötter et al., 2014; Rémy et al., 2017), challenging the retrievals of HCHO VCDs from space by complicating the assumed vertical profiles of HCHO and aerosols. On the one hand, aerosols could increase or decrease the sensitivity of the total column to HCHO, depending on the relative distribution of the aerosol layer (Castellanos et al., 2015; Jung et al., 2019; Leitão et al., 2010). On the other hand, aerosols could be potentially misidentified as clouds (Gonzi et al., 2011), thus introducing uncertainties to HCHO retrievals. Aerosol composition may also complicate satellite retrievals (Kwon et al., 2017). Therefore, HCHO retrievals appear to show considerable biases during fire seasons. For example, the OMI Harvard-Smithsonian (SAO) HCHO retrieval (version 3) is biased by −44.5 % to −53.7 % in the Western United States, likely due to wildfires (Zhu et al., 2020). Nevertheless, systematic validation of currently available HCHO retrievals specifically during intense fire seasons remains critically limited.

Previous validation exercises generally directly compare coincident satellite pixels with ship-based, airborne, and ground-based observations. For instance, GOME-2 HCHO data over the remote ocean agrees with ship-based Multi-Axis Differential Optical Absorption Spectroscopy (MAX-DOAS) observations (Peters et al., 2012); OMI HCHO data is 37 % lower than aircraft observations over the Guyanas (Barkley et al., 2013); OMI and GOME-2A/B HCHO retrievals suggest an underestimation of 20 % compared with ground-based measurements in Wuxi, China (Wang et al., 2017). Furthermore, the extensive global networks, including the Fourier Transform InfraRed (FTIR) and MAX-DOAS instruments, have been applied to validate satellite retrievals (De Smedt et al., 2021; Vigouroux et al., 2020). Together they show that observations from the TROPOMI instrument are biased low (−25 %) for regions with elevated HCHO VCDs ($>8.0 \times 10^{15}$ molecules cm^{-2}), while no statistically significant bias is observed for HCHO VCDs in the moderate range ($\sim 5.0 \times 10^{15}$ molecules cm^{-2}). At clean FTIR sites, TROPOMI HCHO VCDs are positively biased (+26 %) relative to ground-based measurements for VCDs below 2.5×10^{15} molecules cm^{-2} (Vigouroux et al., 2020). However, such direct validations with ground-based observations face two practical challenges: (1) Validation results are representative only at the local scale; their applicability to broader regions remains uncertain. (2) A large proportion of *in situ* observations cannot be used for validation, considering satellite overpass time.

In earlier work, Zhu et al. (2016, 2020) introduced an indirect validation approach that leverages a chemical transport model (CTM) as a unified framework to facilitate intercomparison among observational datasets. This approach leverages the full aircraft dataset using an observation-constrained model as a temporally aligned proxy for validation, substantially increasing observational coverage and reducing noise compared to strict coincidence-based comparisons. Following the methodology outlined above, and aiming to address the critical gap in HCHO validation during fire-influenced seasons, we validate five HCHO retrievals from OMI, OMPS-NPP, OMPS-N20, and TROPOMI using *in situ* aircraft observations from the FIREX-AQ and WE-CAN aircraft campaigns, as discussed below.

Here, we focus on validating the performance of satellite HCHO products in their typical application context. Since satellite HCHO data are most commonly used in aggregated forms (e.g., monthly or seasonal averages) for emission inversion and trend analysis, our validation approach targets the accuracy of these spatially and temporally averaged values, rather than instantaneous pixel-level retrievals. While this validation smooths sub-grid fire heterogeneity and plume-scale features, it provides an observation-constrained estimate of satellite biases that is representative of the spatially and temporally averaged conditions under which these data are typically applied.

2. HCHO observations from FIREX-AQ and WE-CAN aircraft campaigns

The FIREX-AQ aircraft campaign, with four aircraft (NASA DC-8 and ER-2, plus two NOAA Twin Otters), deployed a full array of instruments to investigate how fires impact air quality, weather, and climate in summer of 2019. Fig. 1a presents the trajectories of aircraft during the FIREX-AQ campaign. The campaign operated in two phases to capture distinct fire regimes. During the first phase (22 July to 18 August, based

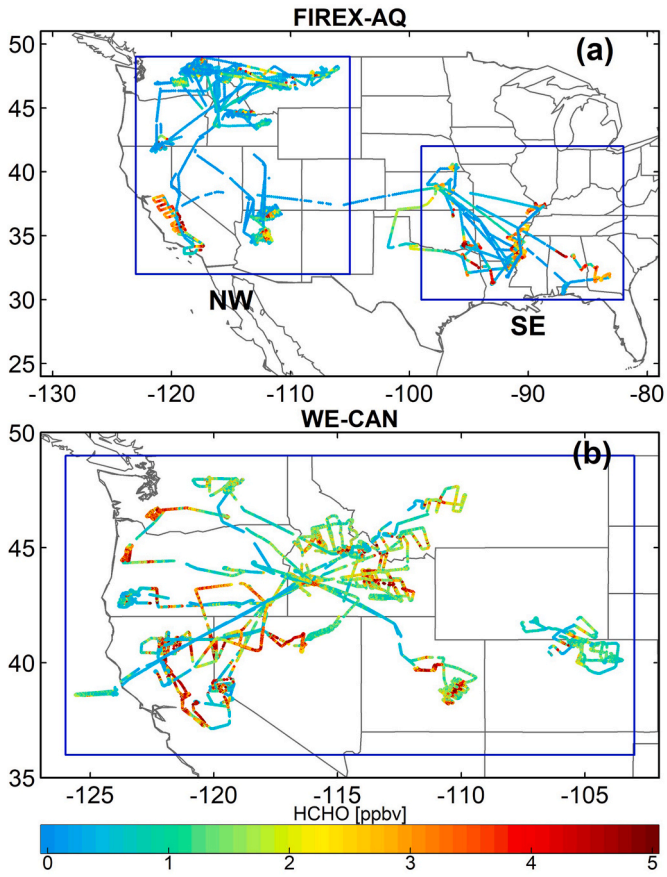

Fig. 1. Flight tracks used in this study. Panel (a) shows flight tracks of FIREX-AQ campaign. This campaign is divided into the southeast (SE) and the northwest (NW) study regions. Panel (b) shows flight tracks of WE-CAN campaign. The three study regions are marked as blue rectangles. HCHO mixing ratios along the aircraft flight paths are indicated by colored points. In the study, we focus only on flight-sampled grid cells in the study regions. The color bar is capped at 5 ppbv (maximum: 145.35 ppbv).

in Boise, Idaho), the DC-8 conducted 15 research flights focusing on wildfires in the northwestern (NW) United States. In this region, the aircraft sampled approximately 14 discrete large-scale wildfires across Washington, Oregon, and Idaho. In contrast, the second phase (19 August to 5 September, based in Salina, Kansas) included 8 research flights investigating numerous smaller prescribed and agricultural fires in the southeastern (SE) United States. This sampling strategy provides a robust dataset covering diverse fire intensities and fuel types.

FIREX-AQ provides extensive observations of chemical species, including carbon monoxide (CO) measured by the Differential Absorption Carbon monOxide Measurement (DACOM) instrument (Sachse et al., 1991), ozone by the NOAA chemiluminescence instrument (Bourgeois et al., 2020), and particle sizes by the laser aerosol spectrometer (LAS) (June et al., 2022). Observations during FIREX-AQ have recently been used in studies such as particle properties and evolution in wildfire smoke (June et al., 2022), generation of secondary pollutants and depletion of nitrogen oxides (Junghenn Noyes et al., 2020), and ozone chemistry as well as HCHO evolution in wildfires (Liao et al., 2021; Xu et al., 2021).

The WE-CAN campaign deployed the NSF/NCAR C-130 research aircraft to characterize the emissions and chemical evolution of wildfire plumes in the western US during summer 2018. Fig. 1 (panel b) shows flight tracks of the WE-CAN campaign. The campaign was conducted in 2018, primarily based in Boise, ID (from 24 July to 31 August), with a final phase in Broomfield, CO (from 1 to 13 September). In total, the C-130 research aircraft conducted 19 flights and sampled smoke from wildfires across seven western states. The core objective was to sample 27 individual fire plumes in the near field (including re-sampling some fires on different days), providing extensive data on the initial chemical transformation and regional smoke aging. Sampling was strategically concentrated between 14:00 and 19:00 local time to capture emissions during the most active burning period (Juncosa Calahorrano et al., 2021; Lindaas et al., 2021; Palm et al., 2021; Permar et al., 2021).

Similar to FIREX-AQ, extensive chemical species were measured during WE-CAN, including CO by quantum cascade laser spectrometry, NO, NO_2, and ozone by the NCAR chemiluminescence instruments (Ridley and Grahek, 1990; Ridley et al., 1992). WE-CAN observations facilitate studies regarding the impact of photochemistry on emissions in fresh plumes (Palm et al., 2021), comparison between field reactive nitrogen measurements and laboratory measurements (Lindaas et al., 2021), and emission estimations of trace gases from wildfires (Permar et al., 2021).

During FIREX-AQ, HCHO was measured by both the Compact Atmospheric Multispecies Spectrometer (CAMS) (Fried et al., 2020; Richter et al., 2015) and In Situ Airborne Formaldehyde instrument (ISAF) (Cazorla et al., 2015). The instrument accuracy is 4 % (Richter et al., 2015) and 10 % (Cazorla et al., 2015), with a respective detection limit of ~40 ppt (Richter et al., 2015) and 36 ppt (Cazorla et al., 2015), for CAMS and ISAF. Fig. 2 shows CAMS observations correlate highly (r = 0.99) with those from ISAF, with a reduced major axis (RMA) regression slope of 0.77 ± 0.00 (ISAF *vs.* CAMS), and a near-zero intercept of −0.01 ± 0.01. This suggests a good application prospect that CAMS and ISAF data are equivalent after bias correction. We use CAMS measurement during FIREX-AQ, given its linear relationship with ISAF measurement and multiple verification methods. In fact, airborne comparisons with the University of Oslo's Proton Transfer Reaction Time-of-Flight Mass Spectrometer (PTR-ToF-MS) on two specific days where the water-vapor back reaction interference was calibration out during the FIREX-AQ study revealed HCHO agreement to within 3.5 %. HCHO was measured during the WE-CAN by PTR-ToF-MS, with an instrument accuracy of 40 % (Permar et al., 2021) and a detection limit of 300 ppt (Zhu et al., 2020).

Spatially, elevated HCHO was measured over regions with intense wildfires, such as Arkansas during FIREX-AQ (SE), central California and Montana during FIREX-AQ (NW), and the western US during WE-CAN

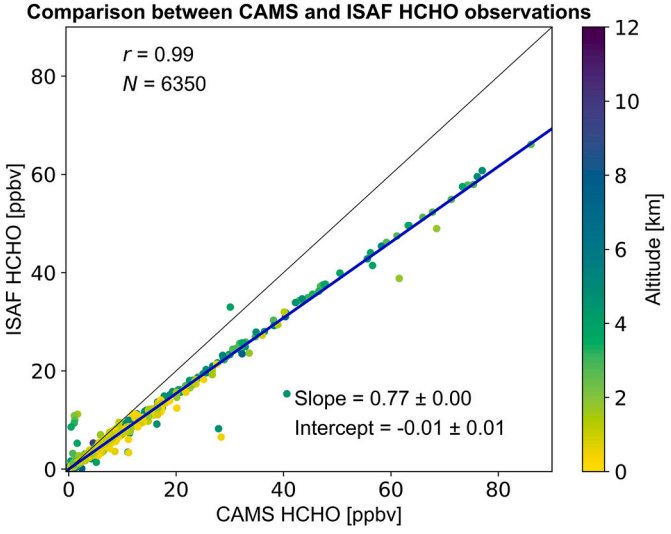

Fig. 2. Point-by-point comparison of 1-min averaged CAMS and ISAF HCHO observations collected aboard the NASA DC-8 during the FIREX-AQ. Data points are color-coded by flight altitude. The reduced major axis (RMA) regression line (blue) is overlaid, with its slope and intercept reported alongside the Pearson correlation coefficient (r) and number of paired samples (N). The 1:1 reference line is shown in black.

(Fig. 1). Vertically, FIREX-AQ (NW) mean HCHO profile is relatively consistent with that from WE-CAN, with enhanced levels between 2 km and 5 km (Fig. 3). We attribute this to primary emission and secondary production from NMVOCs during wildfires, as indicated by the vertical profiles of monoxide carbon (CO) and ozone (Fig. S1). Differently, higher levels of HCHO during FIREX-AQ (SE) are below 2 km and decline quickly at higher altitudes, likely resulting from small agriculture fires and biogenic emissions in this region.

3. GEOS-Chem model as the intercomparison platform

We adopted the GEOS-Chem (v12.9.3) global 3-D CTM as the intercomparison platform to connect aircraft observations with satellite retrievals. We compare satellite observations against aircraft-constrained GEOS-Chem simulations, ensuring temporal consistency by sampling the model at satellite overpass time (~13:30 LT). The GEOS-Chem model contains a detailed tropospheric chemistry mechanism of NO_x-VOCs-ozone-aerosol-halogens (Bey et al., 2001; Zhu et al., 2019), and has been widely used to reproduce observed HCHO variations (Boeke et al., 2011; Chan Miller et al., 2017; Chance et al., 2000; Franco et al., 2015; Zhu et al., 2020).

We conducted high-resolution nested simulations using the GEOS-Chem model over North America (130°W–60°W, 9.75°N–60°N) with a resolution of 0.5° × 0.625° and 47 vertical pressure levels up to 0.01 hPa, and dynamic boundary conditions were updated every 3 h from a global 4° × 5° run. Anthropogenic emissions on the global scale were derived from the Community Emissions Data System (CEDS) (Hoesly et al., 2018), while over North America they were replaced by the 2011 National Emission Inventory (NEI-2011) from the US Environmental Protection Agency (EPA). Biogenic VOC emissions were simulated interactively using the online version of the Model of Emissions of Gases and Aerosols from Nature (MEGAN) (Guenther et al., 2012). Emissions from biomass burning were prescribed using the fourth release of the Global Fire Emissions Database (GFED4) (Giglio et al., 2013). The model simulations were driven by meteorological reanalysis fields from NASA's Modern-Era Retrospective Analysis for Research and Applications, Version 2 (MERRA-2), produced by the Global Modeling and Assimilation Office (GMAO) (Gelaro et al., 2017). To mitigate spin-up artifacts and reduce dependence on initial chemical conditions, the nested and global simulations were initialized with a three-month and twelve-month spin-up period, respectively. Model outputs were temporally and spatially collocated with aircraft measurement tracks by subsampling GEOS-Chem fields along the actual flight trajectories to ensure direct comparability with observational data. This trajectory-based sampling strategy focuses the validation on fire-affected locations—avoiding dilution by background regions and preserving sensitivity to the systematic satellite biases that manifest under elevated HCHO conditions.

As illustrated in Fig. 3, the GEOS-Chem model underestimates HCHO from fires, *i.e.*, between 2 km and 5 km during FIREX-AQ (NW) and WE-CAN and below 2 km during FIREX-AQ (SE). This is likely due to the uncertainties associated with the GFED4 fire emission inventory and other model errors. Although NMVOC speciation may affect HCHO vertical distribution, aircraft-constrained scaling of total fire HCHO helps mitigate biases in the effective fire HCHO emission factor. We also use the Global Fire Assimilation System (GFAS; Kaiser et al., 2012) fire emission inventory, which barely improves the GEOS-Chem simulations (Fig. S2). Fire emission inventories are highly uncertain owing to a limited understanding of the emitted amount and species, both spatially and temporally (Baker et al., 2018; Faulstich et al., 2022; Jin et al., 2022; Permar et al., 2023; Wolfe et al., 2022), with varying degrees of underestimations in fire emissions (Faulstich et al., 2022; Hawbaker et al., 2017; Yamasoe et al., 2015; Zeng et al., 2016). By integrating mean vertical HCHO profiles, GEOS-Chem is respectively biased by −67.5 %, −23.0 %, and −62.1 % during FIREX-AQ (NW), FIREX-AQ (SE), and WE-CAN. Those regional biases are used as correction factors in validating satellite HCHO retrievals.

4. Satellite HCHO products

Table 1 summarizes currently available satellite HCHO products from OMI, OMPS-NPP, OMPS-N20, and TROPOMI. Those products are different in their SCD fitting and VCD computing. Here we will briefly describe each product following retrieval documents.

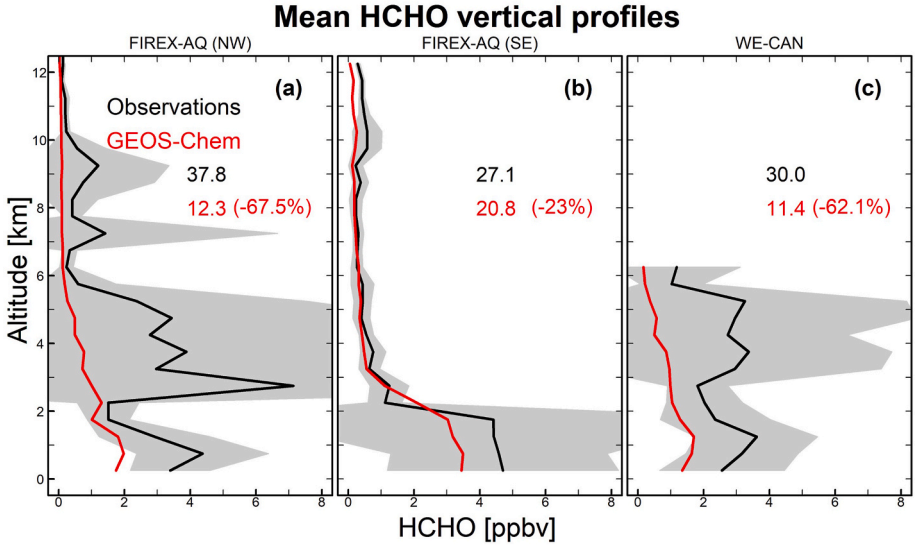

Fig. 3. Observed and GEOS-Chem modeled mean HCHO vertical profiles during FIREX-AQ (NW), FIREX-AQ (SE), and WE-CAN, corresponding to Panel (a), (b), and (c), respectively. GEOS-Chem simulations are sampled at 1-min temporal resolution along the flight paths to correspond with the spatiotemporal coordinates of the aircraft observations. In this study, we focus only on values within the study regions, as shown in blue rectangles in Fig. 1. HCHO concentrations are vertically averaged in 500 m bins to derive mean vertical profiles, with shaded areas representing the standard deviation of observations. Observed vertical column densities (Observations; in a unit of 10^{15} molecules cm^{-2}) are calculated using the mean observed profiles (black lines), together with pressure and temperature. Modeled HCHO column densities from GEOS-Chem (in a unit of 10^{15} molecules cm^{-2}) are computed by vertically integrating the simulated HCHO mixing ratio profiles. Numbers in parentheses indicate the relative biases of GEOS-Chem VCDs compared to observations, which are subsequently used as correction factors for the modeled VCDs.

Table 1
Satellite HCHO products intercompared and validated in this study.

Retrieval	Nadir resolution (km^2)	Local overpass time	Fitting windows (nm)	CTM
OMI-SAO (v3)	24 × 13	13:30	328.5–356.5	GEOS-Chem v09-01-03
OMI-SAO (v4)	24 × 13	13:30	328.5–356.5	GEOS-Chem v09-01-03
OMPS-SAO (NPP)	50 × 50	13:30	328.5–356.5	GEOS-Chem v09-01-03
OMPS-SAO (N20)	17 × 17 12 × 17 (since February 13, 2019)	13:30	328.5–356.5	GEOS-Chem v09-01-03
TROPOMI-BIRA	3.5 × 7 3.5 × 5.5 (since August 6, 2019)	13:30	328.5–359	TM5-MP

HCHO products used in this study, containing five products from four sensors (OMI, TROPOMI, OMPS-NPP, and OMPS-N20). OMI and OMPS products are from Smithsonian Astrophysical Observatory (SAO), and TROPOMI product is from the Belgian Institute for Space Aeronomy (BIRA). The CTM generates HCHO shape factors (normalized vertical mixing ratio profiles) and provides the background-correction (VCD_0; see in Eq. (1)) applied in corresponding products. The local overpass time is close for all satellites, making intercomparison possible.

4.1. OMI-SAO v3 and v4 products

OMI, launched aboard NASA's Aura satellite on July 15, 2004, has delivered global HCHO observations in the early afternoon on a daily basis, with a nadir spatial resolution of 24 × 13 km^2. Currently, two operational HCHO retrieval algorithms are available from OMI: (1) the NASA official product from the Smithsonian Astrophysical Observatory (SAO) (González Abad et al., 2015); (2) the European Union Quality Assurance for Essential Climate Variables (QA4ECV) product (De Smedt et al., 2015; Zara et al., 2018). Here, we focus on NASA official product, namely OMI-SAO (v3) and its updated version (v4).

OMI-SAO (v3) retrieves slant column densities (SCDs) by performing spectral fitting of radiances using the Basic Optical Absorption Spectroscopy (BOAS) method (Chance, 1998; González Abad et al., 2015). Then, a reference-sector-based correction is implemented toaccount for retrieval biases associated with selecting the Pacific region as the reference spectrum. Finally, reference-sector-corrected SCD is converted to VCD using AMF, as shown in Eq. (1).

$$VCD = \frac{SCD - Correction}{AMF} \quad (1)$$

The typical fitting uncertainty of VCD ranges from 45 % to 100 %, which would be reduced to 30 % under high-concentration conditions (González Abad et al., 2015). Previously, OMI-SAO (v3) has been widely used in characterizing biogenic VOCs (Curci et al., 2010; Liu et al., 2018; Millet et al., 2008; Wang et al., 2022) as well as fire and anthropogenic emissions (Bauwens et al., 2016; Li et al., 2022; Liu et al., 2018; Shen et al., 2019; Zhu et al., 2017a), inferring cancer risks in the US (Zhu et al., 2017b), investigating ozone chemical production regime (Jung et al., 2022), mapping total-column OH throughout the remote troposphere (Wolfe et al., 2019), and examining information on the global composition of aerosol particles (Veefkind et al., 2011).

For OMI-SAO (v4) HCHO product, all terms are listed in Eq. (2). The HCHO SCD (dSCD) represents a differential SCD between the slant column retrieved from the measurement spectrum and that derived from a reference spectrum over a relatively clean region. Therefore, the HCHO background (Ref) needs to be compensated, which is estimated from a CTM. In addition, biases in the HCHO slant column that depend on latitude and solar zenith angle are corrected using modeled HCHO values (Bias) (Ayazpour et al., 2025).

$$VCD = \frac{dSCD + Ref + Bias}{AMF} \quad (2)$$

4.2. OMPS-SAO (NPP) and OMPS-SAO (N20) products

The first OMPS aboard NASA Suomi-NPP (OMPS-NPP) satellite launched in October 2011, and the second OMPS on NOAA-20 (OMPS-N20) launched in November 2017, provide environmental data globally at nadir views. OMPS-N20 and OMPS-NPP both have overpass times of ~13:30. Compared with OMI, OMPS-NPP, and OMPS-N20 have reduced spectral resolutions (1 nm) but improved signal-to-noise ratio (SNR). OMPS-NPP has a spatial resolution of 50 × 50 km^2. OMPS-N20 has a finer resolution at nadir of 17 × 17 km^2 (prior to mid-February 2019) or 17 × 12 km^2 (afterwards) but at the expense of lower SNR relative to that of OMPS-NPP. Previously, several HCHO products from OMPS have been released (González Abad et al., 2016; Li et al., 2015; Su et al., 2019). For the OMPS-SAO (NPP) and OMPS-SAO (N20) HCHO products used in this paper, they adopt a similar retrieval algorithm as OMI-SAO (v4), with all terms summarized in Eq. (2).

The systematic uncertainty of OMPS-SAO in slant column fitting is similar to that of other HCHO retrievals at ~20 % (De Smedt et al., 2018), as are uncertainties in the AMFs. The OMPS retrievals differ in one significant way from those of OMI and TROPOMI in that they use a climatological cloud top pressure due to a lack of operational cloud products from OMPS-N20. Uncertainties in the cloud pressure may introduce errors in the AMFs on the order of 15 % in regions without biomass burning (Nowlan et al., 2023).

Previous studies have leveraged OMPS observations to constrain VOC emissions (Choi et al., 2022), attribute ambient formaldehyde to its primary and secondary sources (Su et al., 2019), diagnose ozone production regimes (Souri et al., 2020), and assess associated health impacts (Su et al., 2022).

4.3. TROPOMI-BIRA product

TROPOMI onboard the Copernicus Sentinel-5 Precursor satellite launched on October 13, 2017, delivers daily global measurements of atmospheric trace gases with a spatial resolution of 3.5 × 7 km^2 (updated to 3.5 × 5.5 km^2 since August 2019). Spectral resolution and SNR of TROPOMI are equivalent to those of OMI. The TROPOMI-BIRA retrieval is based on the DOAS method, following the QA4ECV retrieval algorithm (De Smedt et al., 2018). Briefly, the SCD is retrieved in a fitting interval of 328.5–359 nm. To remove systematic offsets with temporal and latitudinal dependence, a reference sector correction is implemented to yield the corrected SCD (SCD_c; De Smedt et al., 2018; Khokhar et al., 2005). Then SCD_c is converted to VCD using a corresponding AMF and a background correction (VCD_0), the vertical column from the TM5 CTM (Huijnen et al., 2010; Williams et al., 2017) in the reference sector.

$$VCD = \frac{SCDc}{AMF} + VCD_0 \quad (3)$$

For TROPOMI-BIRA HCHO VCDs, the systematic uncertainty is less than 40 % (ESA, 2021). Due to its unparalleled horizontal resolution, TROPOMI-BIRA product has been widely used previously, including analyzing the patterns and origins of summertime HCHO in Alaska (Zhao et al., 2022), interpreting the effects of the COVID-19 lockdown on air quality from city to global scales (Levelt et al., 2022; Sun et al., 2021), identifying HCHO and its source during wildfires (Alvarado et al., 2020), and exploring the response of anthropogenic NMVOC emissions to urbanization in Asia (Pu et al., 2022). More recently, its performance under high anthropogenic VOC levels and aerosol-rich conditions was further evaluated in the photochemically active Greater Bay Area of

southern China (Zhao et al., 2025).

4.4. AMF calculation

All products above require an AMF, which is determined from the observation's geometric information (solar zenith angle θ_Z and satellite viewing zenith angle θ_V), *a priori* profile of HCHO, cloud properties, and optical scattering characteristics of the atmosphere and surface. The formulation of AMF in Eqs. (4) and (5) is widely employed (De Smedt et al., 2018; González Abad et al., 2015, 2016; Zhao et al., 2022; Zhu et al., 2016). It involves retrieving a geometrical AMF (AMF_G) to account for the viewing geometry in a non-scattering atmosphere, followed by a correction where scattering weights w are applied to the normalized vertical shape factors S (Palmer et al., 2001).

$$AMF_G = \frac{1}{\cos\theta_z} + \frac{1}{\cos\theta_v} \tag{4}$$

$$AMF = AMF_G \int_{p_s}^{0} w(p) S(p) d_p \tag{5}$$

The integration in Eq. (5) is implemented at pressure (p) coordinates from the surface (p_s) to the top of the atmosphere. The shape factor S is the normalized profile of mixing ratio $C(p)$:

$$S_{(p)} = \frac{C_{(p)} VCD_A(p)}{\int_{P_s}^{0} C_{(p)} VCD_A(p) d_p} \tag{6}$$

where VCD_A (p) is the partial air column at vertical pressure p.

Satellite HCHO products listed in Table 1 provide VCD, SCD, AMF, AMF_G, $S(p)$ or *a priori* gas profile, and $w(p)$ or the equivalent averaging kernels $A(p) = w(p)/AMF$ (De Smedt et al., 2018). To further explore which factor might dominate the retrieval bias, we recompute AMF using mean profiles from aircraft campaigns provided in satellite products following Eq. (5). In this study, we select level-2 pixels using the following criteria: (1) data quality tests (quality value $\geq$ 0.5 for TROPOMI-BIRA, main data quality flag = 0 for other products), (2) cloud fraction less than 0.3, (3) VCD from -5.0×10^{15} to 1.0×10^{17} molecules cm^{-2}, (4) and solar zenith angle less than 60°.

5. Intercomparison of satellite HCHO products during FIREX-AQ and WE-CAN

As shown in Fig. 4, satellite HCHO VCDs vary consistently among the five products during WE-CAN. The daily variations are primarily in line with fire activities and surface temperature. For instance, HCHO column decreases from ~1.2×10^{16} molecules cm^{-2} to ~0.8×10^{16} molecules cm^{-2} from July to September, when fire activity shrinks by ~60 %. The correlation coefficients (r) between HCHO VCDs and fire counts range from 0.19 (OMI-SAO v3 and v4) to 0.67 (TROPOMI-BIRA), higher than those between HCHO VCDs and surface temperature with correlation coefficients ranging from −0.20 (OMI-SAO v3) to 0.49 (OMPS-SAO NPP), implying that fire rather than biogenic emission is the main driver of HCHO VCDs during this period. Among all products, TROPOMI-BIRA (r = 0.67) and OMPS-SAO N20 (0.66) show better performance, likely due to their higher SNR (TROPOMI) and finer spatial resolutions (TROPOMI and OMPS-N20). OMI-SAO (v3) retrieval performs the worst, possibly relevant to the instrumental degradation of OMI (Baek et al., 2014). The OMI instrument is the same in OMI v3 and v4, while the reason for the poor performance of OMI v3 in comparison with v4 is the flagging scheme of OMI v3 radiances that was rejecting many spectral pixels that were still useful. Observations from the FIREX-AQ campaign are too sparse and scattered to make a similar analysis.

Fig. 5–6 and S4–S7 demonstrate the spatial distribution of HCHO VCDs from the five products and GEOS-Chem during the two aircraft campaigns. Spatial correlation coefficients among satellite products during the flight campaigns are summarized in Tables 2, S1, and S2. Most of the products capture high values over the southeast US during FIREX-AQ (SE) and the northwest US during WE-CAN and FIREX-AQ (NW). Correlation coefficients between satellite products with aircraft-constrained GEOS-Chem (denoted as corrected GC for brevity) range from −0.07 (OMI v3) to 0.82 (TROPOMI-BIRA) during FIREX-AQ (NW), from 0.16 (OMI v3) to 0.65 (OMPS-N20) during FIREX-AQ (SE), and from 0.17 (OMI-SAO v3) to 0.86 (TROPOMI-BIRA) during WE-CAN. Newly released HCHO products (*i.e.*, OMI-SAO v4, OMPS-SAO NPP, OMPS-SAO N20, and TROPOMI-BIRA) generally show higher consistency with each other during WE-CAN, with spatial correlation coefficients from 0.57 to 0.84. This is likely driven by their higher SNR, finer horizontal resolutions, and/or updated retrieval algorithms.

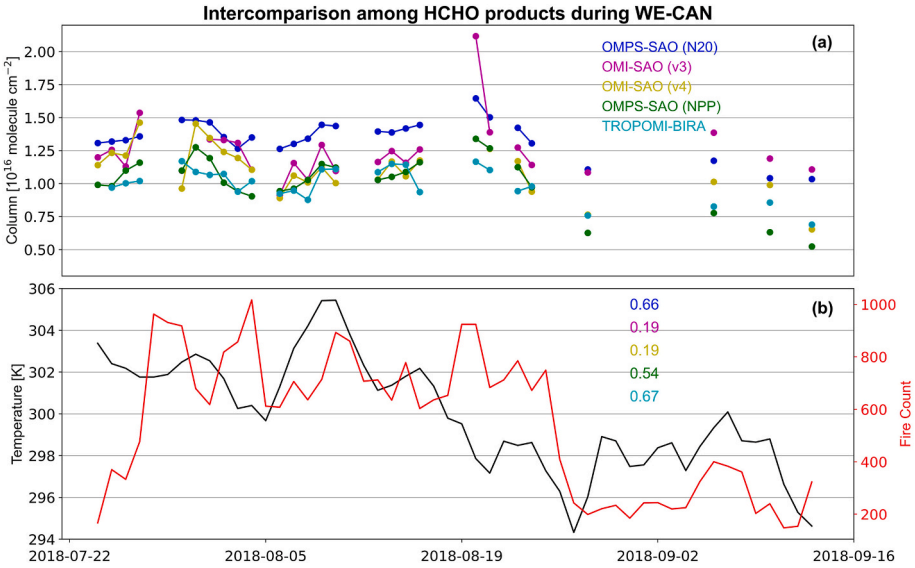

Fig. 4. Time series of HCHO VCDs from different products intercompared with surface temperature and NPP VIIRS fire count during WE-CAN. Panel (a) displays daily mean HCHO column densities averaged over the study region (outlined by the rectangle in Fig. 1b) for five satellite retrievals. Panel (b) shows MERRA-2 daily surface temperature (black line) at 13:00–14:00 (local time) averaged over the study region, along with fire counts from NPP NASA VIIRS Thermal Anomalies/Fire product. The fire count is calculated as the sum of points with firemask more than 7, a threshold representing high confidence in fires. Temporal correlation coefficients (r) between daily HCHO VCDs and fire counts are shown in color.

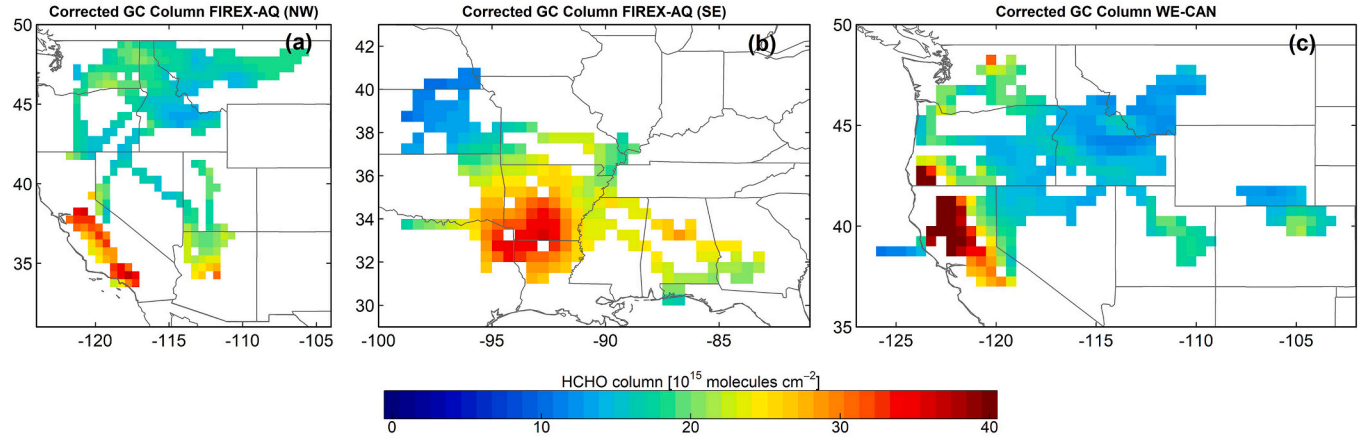

Fig. 5. Corrected GEOS-Chem HCHO vertical column densities along corresponding flight tracks. Panel (a) shows data averaged during FIREX-AQ (NW; 22 July–18 August 2019). Panel (b) shows data during FIREX-AQ (SE; 20 August-5 September 2019). Panel (c) shows data during WE-CAN (24 July–13 September 2018). GEOS-Chem simulations are temporally and spatially aligned with satellite overpasses during the respective campaigns and adjusted using a bias correction factor derived from aircraft observations (Fig. 3). The corrected GEOS-Chem results are then regridded onto 0.5° × 0.5° grids. In this study, validation and intercomparison results are limited to the colored grids, which are sampled by aircraft (consistent with flight tracks from Fig. 1). The color bar saturates at 4.0×10^{16} molecules cm^{-2}.

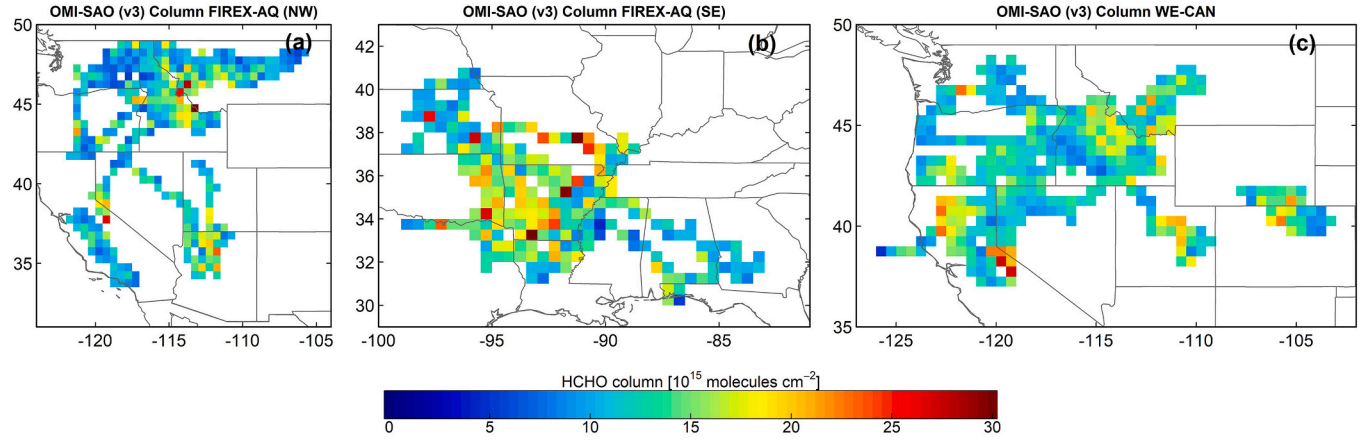

Fig. 6. OMI-SAO (v3) HCHO vertical column densities along corresponding flight tracks. Panel (a) shows data averaged during FIREX-AQ (NW; 22 July–18 August 2019). Panel (b) shows data during FIREX-AQ (SE; 20 August-5 September 2019). Panel (c) shows data during WE-CAN (24 July–13 September 2018). The color bar saturates at 3.0×10^{16} molecules cm^{-2}.

Table 2
Spatial correlation coefficients (*r*) among HCHO products during FIREX-AQ (NW).

HCHO column	OMI-SAO (v3)	OMI-SAO (v4)	OMPS-SAO (NPP)	OMPS-SAO (N20)	TROPOMI-BIRA
OMI-SAO (v4)	0.41*	–	–	–	–
OMPS-SAO (NPP)	0.16*	0.25*	–	–	–
OMPS-SAO (N20)	0.22*	0.29*	0.34*	–	–
TROPOMI-BIRA	−0.05 (0.12)	0.12*	0.17*	0.39*	–
Corrected GEOS-Chem	−0.07*	0.23*	0.28*	0.34*	0.82*

Spatial correlation coefficients between different pairs of HCHO VCDs from satellite products and GEOS-Chem. The correlation coefficients are calculated by applying temporally mean data on the sampled 0.5° × 0.5° grids (colored grids) during FIREX-AQ (NW) in Figs. 5 and 6, and S4–S7. Spatial correlation coefficients during other campaigns are in Tables S1 and S2. Correlation coefficients with $p < 0.05$ are marked with*; exact p-values are reported otherwise. Sample sizes (N) is 328. The p-values are derived from point-to-point correlations without explicitly accounting for spatial autocorrelation.

As shown in Fig. 5–6 and S4–S7, all products are biased low relative to corrected GC results. The model is temporally and spatially aligned with satellite observations and corrected based on its bias relative to aircraft data (Fig. 3). Table 3 summarizes the biases of OMI-SAO (v3) compared with corrected GC results along the sampled grids during FIREX-AQ and WE-CAN. Similarly, biases for other retrievals are listed in Table S3–S6. Given that satellite products adopt different algorithms, we validate each one to examine the source of the biases, as discussed below.

6. Validation of satellite HCHO products during FIREX-AQ and WE-CAN

6.1. OMI-SAO v3 and v4 products

For OMI-SAO (v3), the biases range from −25.0 % to −37.4 % (Table 3) compared with corrected GC HCHO VCDs. While for OMI-SAO (v4), biases range from −27.5 % to −47.7 % (Table S3). OMI-SAO (v3) shows mildly lower biases, probably due to higher fitted SCDs with possibly unresolved drift and lower reference sector corrections, as implied by Eq. (1). The difference in AMFs might also contribute to the discrepancy between the products, as listed in Table 3 and S3.

Table 3
OMI-SAO (v3) HCHO columns during FIREX-AQ and WE-CAN.

Campaign	Mean values						With aircraft shape factors		Corrected GEOS-Chem
	SCD	Correction	AMF	AMF_G	VCD	VCD_m	AMF_r	VCD_r	VCD_c
FIREX-AQ (NW)	14.12	2.63	1.08	2.59	11.93 (-37.4 %)	10.67 (-44.0 %)	1.19	9.65 (-49.4 %)	19.06
FIREX-AQ (SE)	16.21	3.32	0.98	2.64	13.64 (-34.0 %)	13.12 (-36.5 %)	0.97	13.30 (-35.6 %)	20.66
WE-CAN	16.18	3.36	1.14	2.61	12.40 (-25.0 %)	11.25 (-31.9 %)	1.23	10.33 (-40.7 %)	16.53

Mean values are calculated spatially and temporally applying the grids sampled by aircraft (colored grids during FIREX-AQ and WE-CAN in Fig. 5–6. HCHO columns including VCD, VCD_m, VCD_r, and VCD_c are in unit of 10^{15} molecules cm^{-2}, while AMFs are dimensionless. Biases relative to the corrected GC column (VCD_c) are provided in parentheses. Mean values SCD, Correction, AMF, and VCD are obtained by direct averaging of valid satellite pixels. VCD_m is recomputed using the mean SCD, Correction, and AMF following Eq. (1). AMF_r is recalculated from the mean AMF_G, the observed HCHO shape factor from the CAMS instrument or PTR-ToF-MS instrument, and the scattering weights or averaging kernels from the satellite product (Fig. 7) according to Eq. (5). VCD_r is recomputed using mean SCD, AMF_r, and Correction by Eq. (1).

We follow Eq. (5) to update AMF (AMF_r in Table 3) by replacing satellite HCHO profiles with observed profiles from aircraft (Fig. 3) and with scattering weights from the satellite product (Fig. 7). As for OMI-SAO (v3), we recompute VCD (VCD_r in Table 3) with mean SCD, updated AMF (AMF_r), and mean Correction following Eq. (1). Comparing VCD_r with VCD_m (recomputed VCD using mean SCD, AMF, and Correction following Eq. (1)), we find no significant improvement in biases during any aircraft campaign, implying that shape factors may not be the main driver of biases. Therefore, a large part of the resulting retrieval biases may be traced to the fitted SCD (SCD), reference sector correction (Correction), or AMF calculation involving the scattering properties.

In like manner, we find OMI-SAO (v4) retrieval biases might mainly stem from the differential SCD (dSCD), latitude-dependent bias (Bias), or AMFs involving the scattering properties. Notably, we find that the background correction (Ref) contributes significantly (~40 %) to the total column (VCD). The background correction is roughly consistent (~4.0×10^{15} molecules cm^{-2}), which is in line with the observed HCHO VCDs (2.0×10^{15} molecules cm^{-2} to 4.6×10^{15} molecules cm^{-2}) measured over remote Pacific Ocean (De Smedt et al., 2008; González Abad et al., 2015; Singh et al., 2009; Wolfe et al., 2019).

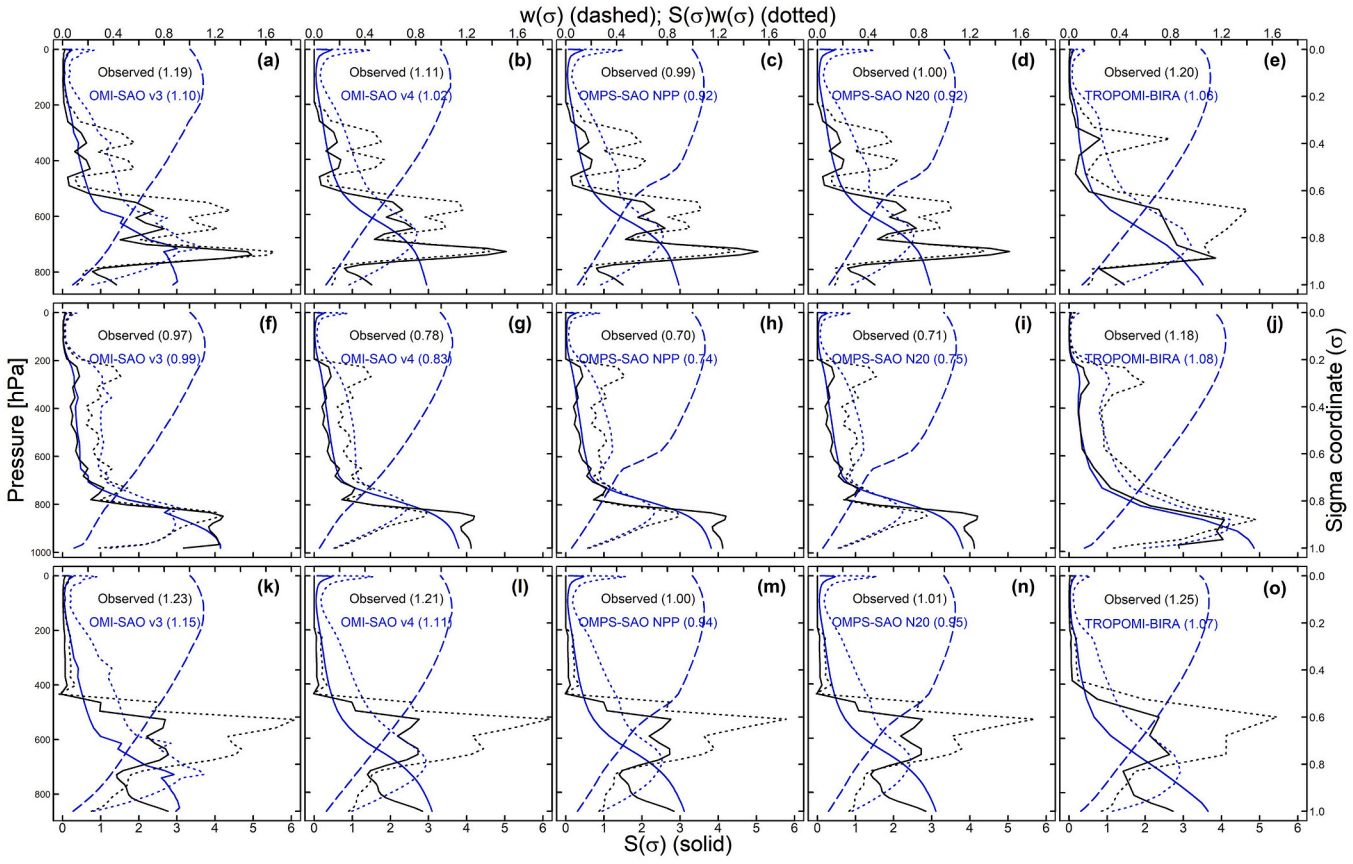

Fig. 7. Air mass factor (AMF) components of the five satellite products (OMI-SAO v3, OMI-SAO v4, OMPS-SAO NPP, OMPS-SAO N20, and TROPOMI-BIRA) over FIREX-AQ (NW), FIREX-AQ (SE), and WE-CAN campaigns are shown in panels (a–e), panels (f–j), and panels (k–o), respectively. Each panel presents the campaign-averaged scattering weight (*w*, dashed blue) and shape factor (*S*, solid blue) from satellite retrievals, computed over the aircraft-sampled grid cells (colored in Fig. 5). Their product (dotted blue), which—when vertically integrated using Eq. (3)—yields the mean AMF, is also shown. Observed HCHO shape factors (black solid) are calculated from the mean vertical profiles in Fig. 3, specific to each campaign. For the WE-CAN, profiles from ATom-1 and ATom-2 (Fig. S3) are used to extend observations above 6 km. All observed HCHO shape factors are projected to the corresponding satellite vertical resolutions. Additionally, the product of the satellite-derived scattering weight (dashed blue) and the observed HCHO shape factor (black solid) is plotted (dotted black). Integrated mean AMF values—computed using either satellite (blue) or observed (black) shape factors—are provided in the legend.

6.2. OMPS-SAO (NPP) and OMPS-SAO (N20) products

As shown in Table S4–S5, OMPS-SAO (NPP) is biased by −31.5 % to −56.7 %, and OMPS-SAO (N20) is biased by −11.0 % to −28.3 %, compared with the corrected GC HCHO VCDs. The better performance of OMPS-SAO (N20) is likely due to the fact that OMPS-SAO (N20) product has higher fitted SCDs (dSCD). Although with varying overpass times, different spatial resolutions and SNRs might cause discrepancies in retrieved SCD between OMPS-NPP and OMPS-N20. The enhancement compensation in latitude-dependent bias (Bias) of OMPS-SAO (NPP) affects the discrepancy slightly.

Recomputed VCDs (VCD_r) for OMPS-SAO (NPP) and OMPS-SAO (N20) are listed in Tables S4–S5. We find that most of the recomputed results show no significant change except for OMPS-SAO (N20) during FIREX-AQ (SE). This indicates that *a priori* HCHO profile might have the potential to improve HCHO retrievals when AMFs are low and SCDs are high. We attribute product bias mainly to the fitted SCD (dSCD) and AMF related to scattering factors, with a nonnegligible impact from the latitude-dependent bias (Bias) term.

6.3. TROPOMI-BIRA product

TROPOMI-BIRA is based by −38.7 % to −49.4 % compared with corrected GC HCHO VCDs. Generally, TROPOMI-BIRA presents a relatively large bias compared to other products during each campaign (Table 3 and S3–S5). As implied in Eq. (3), those biases are from the corrected SCD (SCD_c), AMF, or background correction (VCD_0). Table S6 summarizes the mean values of those terms, highlighting the impacts of low SCDs and high AMFs.

Likewise, we recomputed VCD (VCD_r Table S6) with mean SCD_c, updated AMF (AMF_r), and mean VCD_0 following Eq. (3). Comparing VCD_r with VCD_m, we find no significant improvement in the biases during any aircraft campaign. Therefore, we conclude that shape factors may not be the main contributor to TROPOMI-BIRA biases. A large part of the resulting biases may be traced to the corrected SCD (SCD_c) or AMF calculation involving the scattering properties. The background corrections (VCD_0; $\sim 4.0 \times 10^{15}$ molecules cm^{-2}) account for a large proportion (>40.0 %), implying it might provide a potential for improvement in TROPOMI-BIRA product.

Fig. 7 compares vertical AMF components (shape factors and scattering weights) from the five satellite products.We see OMI-SAO (v3), OMI-SAO (v4), OMPS-SAO (NPP), and OMPS-SAO (N20) capture vertical variations of shape factors and scattering weights better compared to TROPOMI-BIRA due to finer vertical spatial resolutions. The observed shape factors are not smooth with some peaks compared to satellite shape factors, which is likely caused by the sampling fire plumes, particularly over the northwestern US. Overall, Fig. 7 demonstrates both the general consistency of vertical AMF structures among satellite products and the potential differences in sensitivity to plume vertical distribution.

6.4. Impact of fire plumes on HCHO retrievals

Aerosol effects are not explicitly accounted for in the HCHO retrieval algorithm; however, it is assumed to be implicitly incorporated through the cloud correction applied to the scattering weights (De Smedt et al., 2012). In this study, we try to examine such an impact by focusing on one single fire plume (Fig. S8), which could provide insights into retrieval biases. The fire plume is observed by NPP VIRRS and TROPOMI around 13:30 LT, 2019-8-7. Fig. S9 shows area-averaged vertical profiles of the aerosol optical depth (AOD) and FIREX-AQ HCHO. We see a noticeable lift of aerosol and HCHO into the free troposphere, with the altitude of elevated aerosol being slightly lower than that of HCHO.

The aerosol effect on AMF calculation is explicitly corrected by including in the VLIDORT radiative transfer calculation the AOD vertical profile from Differential Absorption Lidar (DIAL). We model the aerosol scattering with a single scattering albedo of 0.94 and a Henyey–Greenstein phase function characterized by an asymmetry parameter of 0.69, consistent with typical boreal forest biomass burning aerosol models (Dubovik et al., 2002). Compared with the clear-sky situation, the box-AMFs with explicit aerosol correction increase above the aerosol layer (*i.e.*, albedo effect) and decrease below the aerosol layer (*i.e.*, shielding effect). As shown in Fig. S10, the inclusion of aerosol correction leads to an 18.0 % increase in the tropospheric AMF, assuming HCHO is well mixed and located above the aerosol layer. This implies that TROPOMI-BIRA AMF is underestimated, meaning more underestimation of the product if applied with current SCD. Therefore, we suggest that shape factors and aerosol scatterings may not be the main drivers of TROPOMI-BIRA retrieval biases, and further improvement may focus on SCD fitting or other scattering factors like surface albedo and clouds.

7. Conclusions

We have used HCHO observations from FIREX-AQ and WE-CAN flight campaigns, combined with the nested GEOS-Chem model simulations at a 0.5° × 0.625° horizontal resolution, to intercompare and validate five satellite HCHO products from OMI, OMPS-NPP, OMPS-N20, and TROPOMI. Through intercomparison among products, fire activity rather than surface temperature could be the primary factor of variations in HCHO VCDs in the study regions. Nearly all satellite products show HCHO high values over the southeastern and western US, consistent with GEOS-Chem. This systematic, campaign-level evaluation addresses a critical need to understand the behavior of operational satellite HCHO products specifically under intense fire-influenced atmospheric conditions, a context previously lacking robust validation.

Compared with aircraft-informed GEOS-Chem, all satellite products underestimate HCHO VCDs by 11.0 %–56.7 %. OMPS-SAO (N20) product during FIREX-AQ has the lowest bias likely attributed to high SCD and low AMF, while OMPS-SAO (NPP) product has the highest bias mainly suggesting a role for low SCD. By recomputing VCDs with mean terms, we find there is no significant improvement in most cases, which reflects a large contribution to satellite biases derived from the SCD fitting and scattering-weights-involved AMF.

During a single wildfire plume observed during FIREX-AQ, we find aerosol scattering increases AMF. This implies an even more underestimation of the TROPOMI-BIRA product. Therefore, we argue that shape factors and aerosols may not be the main contributors to the biases in TROPOMI-BIRA. Further improvement remains in SCD fitting and other scattering factors in TROPOMI-BIRA product.

Overall, it is important to acknowledge the limitations of our indirect validation approach. The reliability of our results depends on the representativeness of the aircraft observations for the broader fire conditions during the campaigns, and the assumption that the model bias characterized in the flight regions is applicable to the larger satellite pixels. Furthermore, the aircraft-constrained model, while informed by observations, still inherits the underlying physics and chemistry of the GEOS-Chem model. In addition, uncertainties in cloud screening, particularly the potential misclassification of dense wildfire aerosols as clouds, may bias AMF calculations and contribute to inter-satellite differences. Therefore, our findings should be interpreted as providing valuable insights into the relative performance of satellite HCHO products under fire conditions, highlighting potential systematic low biases and their likely origins, rather than definitive absolute truth values. Future retrieval development should focus on improving aerosol scattering representation and reducing slant-column uncertainties, which will help minimize systematic biases during fire events.

CRediT authorship contribution statement

Shuai Sun: Writing – review & editing, Writing – original draft, Visualization, Validation, Methodology, Investigation, Formal analysis, Data curation. **Yuzhong Zhang:** Writing – review & editing. **Song Liu:**

Writing – review & editing, Software. **Lei Shu:** Writing – review & editing, Software. **Isabelle De Smedt:** Writing – review & editing. **Lu Hu:** Writing – review & editing, Resources. **Wade Permar:** Writing – review & editing, Resources. **Dirk Richter:** Writing – review & editing, Resources. **Alan Fried:** Writing – review & editing, Resources. **Lei Zhu:** Writing – review & editing, Visualization, Methodology, Funding acquisition, Conceptualization.

Declaration of competing interest

The authors declare that they have no known competing financial interests or personal relationships that could have appeared to influence the work reported in this paper.

Acknowledgments

This work is funded by the National Natural Science Foundation of China (42375090), Guangdong Provincial Field Observation and Research Station for Coastal Atmosphere and Climate of the Greater Bay Area (2021B1212050024), Major Talent Project of Guangdong Province (2021QN020924), Shenzhen Science and Technology Program (KQTD 20210811090048025), and High-level Special Funds (G03034K006). This work is supported by the Center for Computational Sciences and Engineering at Southern University of Science and Technology. We also gratefully acknowledge the use of satellite observations and aircraft measurements that contributed to this study.

Appendix A. Supplementary data

Supplementary data to this article can be found online at https://doi.org/10.1016/j.atmosenv.2025.121767.

Data availability

The OMI-SAO (v3) HCHO column product is available at https://disc.gsfc.nasa.gov/datasets/OMHCHO_003/summary?keywords=omi%20formaldehyde. The OMPS-SAO (NPP) HCHO column product is available at https://disc.gsfc.nasa.gov/datasets/OMPS_NPP_NMHCHO_L2_1/summary?keywords=omi%20formaldehyde. The OMPS-SAO (N20) HCHO column product is available at https://disc.gsfc.nasa.gov/datasets/OMPS_N20_NMHCHO_L2_1/summary?keywords=omi%20formaldehyde. The TROPOMI-BIRA HCHO column product is available at https://disc.gsfc.nasa.gov/datasets/S5P_L2__HCHO__1/summary?keywords=omi%20formaldehyde. The OMI-SAO (v4) HCHO column product is available upon request. The NPP NASA VIIRS Thermal Anomalies/Fire product is available at https://appeears.earthdatacloud.nasa.gov/task/area. The MERRA-2 data is available at http://geoschemdata.wustl.edu/ExtData. The GEOS-Chem model is available at http://www.geos-chem.org. The FIREX-AQ aircraft campaign is available at https://csl.noaa.gov/projects/firex-aq. The WE-CAN campaign is available at https://www.eol.ucar.edu/field_projects/we-can.

References

Akagi, S.K., Craven, J.S., Taylor, J.W., McMeeking, G.R., Yokelson, R.J., Burling, I.R., Urbanski, S.P., Wold, C.E., Seinfeld, J.H., Coe, H., Alvarado, M.J., Weise, D.R., 2012. Evolution of trace gases and particles emitted by a chaparral fire in California. Atmos. Chem. Phys. 12, 1397–1421. https://doi.org/10.5194/acp-12-1397-2012.

Alvarado, L.M.A., Richter, A., Vrekoussis, M., Hilboll, A., Kalisz Hedegaard, A.B., Schneising, O., Burrows, J.P., 2020. Unexpected long-range transport of glyoxal and formaldehyde observed from the copernicus Sentinel-5 precursor satellite during the 2018 Canadian wildfires. Atmos. Chem. Phys. 20, 2057–2072. https://doi.org/10.5194/acp-20-2057-2020.

Andreae, M.O., Merlet, P., 2001. Emission of trace gases and aerosols from biomass burning. Glob. Biogeochem. Cycles 15, 955–966. https://doi.org/10.1029/2000GB001382.

Ayazpour, Z., González Abad, G., Nowlan, C.R., Sun, K., Kwon, H.-A., Chan Miller, C., Chong, H., Wang, H., Liu, X., Chance, K., O'Sullivan, E., Zhu, L., Vigouroux, C., De Smedt, I., Stremme, W., Hannigan, J.W., Notholt, J., Sun, X., Palm, M., Petri, C., Strong, K., Röhling, A.N., Mahieu, E., Smale, D., Té, Y., Morino, I., Murata, I., Nagahama, T., Kivi, R., Makarova, M., Jones, N., Sussmann, R., Zhou, M., 2025. Aura ozone monitoring instrument (OMI) collection 4 formaldehyde products. Earth Space Sci. 12. https://doi.org/10.1029/2024EA003792 e2024EA003792.

Baek, K.H., Kim, J.H., Park, R.J., Chance, K., Kurosu, T.P., 2014. Validation of OMI HCHO data and its analysis over Asia. Sci. Total Environ. 490, 93–105. https://doi.org/10.1016/j.scitotenv.2014.04.108.

Baker, K.R., Woody, M.C., Valin, L., Szykman, J., Yates, E.L., Iraci, L.T., Choi, H.D., Soja, A.J., Koplitz, S.N., Zhou, L., Campuzano-Jost, P., Jimenez, J.L., Hair, J.W., 2018. Photochemical model evaluation of 2013 California wild fire air quality impacts using surface, aircraft, and satellite data. Sci. Total Environ. 637–638, 1137–1149. https://doi.org/10.1016/j.scitotenv.2018.05.048.

Barkley, M.P., Kurosu, T.P., Chance, K., De Smedt, I., Van Roozendael, M., Arneth, A., Hagberg, D., Guenther, A., 2012. Assessing sources of uncertainty in formaldehyde air mass factors over tropical South America: implications for top-down isoprene emission estimates. J. Geophys. Res. 117, D13304. https://doi.org/10.1029/2011JD016827.

Barkley, M.P., Smedt, I.D., Van Roozendael, M., Kurosu, T.P., Chance, K., Arneth, A., Hagberg, D., Guenther, A., Paulot, F., Marais, E., Mao, J., 2013. Top-down isoprene emissions over tropical South America inferred from SCIAMACHY and OMI formaldehyde columns. J. Geophys. Res. Atmos. 118, 6849–6868. https://doi.org/10.1002/jgrd.50552.

Bauwens, M., Verreyken, B., Stavrakou, T., Müller, J.F., Smedt, I.D., 2022. Spaceborne evidence for significant anthropogenic VOC trends in Asian cities over 2005–2019. Environ. Res. Lett. 17, 015008. https://doi.org/10.1088/1748-9326/ac46eb.

Bauwens, M., Stavrakou, T., Müller, J.F., De Smedt, I., Van Roozendael, M., van der Werf, G.R., Wiedinmyer, C., Kaiser, J.W., Sindelarova, K., Guenther, A., 2016. Nine years of global hydrocarbon emissions based on source inversion of OMI formaldehyde observations. Atmos. Chem. Phys. 16, 10133–10158. https://doi.org/10.5194/acp-16-10133-2016.

Bey, I., Jacob, D.J., Yantosca, R.M., Logan, J.A., Field, B.D., Fiore, A.M., Li, Q., Liu, H.Y., Mickley, L.J., Schultz, M.G., 2001. Global modeling of tropospheric chemistry with assimilated meteorology: model description and evaluation. J. Geophys. Res. 106, 23073–23095. https://doi.org/10.1029/2001JD000807.

Boeke, N.L., Marshall, J.D., Alvarez, S., Chance, K.V., Fried, A., Kurosu, T.P., Rappenglück, B., Richter, D., Walega, J., Weibring, P., Millet, D.B., 2011. Formaldehyde columns from the ozone monitoring instrument: urban versus background levels and evaluation using aircraft data and a global model. J. Geophys. Res. 116. https://doi.org/10.1029/2010JD014870.

Bourgeois, I., Peischl, J., Thompson, C.R., Aikin, K.C., Campos, T., Clark, H., Commane, R., Daube, B., Diskin, G.W., Elkins, J.W., Gao, R.S., Gaudel, A., Hintsa, E. J., Johnson, B.J., Kivi, R., McKain, K., Moore, F.L., Parrish, D.D., Querel, R., Ray, E., Sánchez, R., Sweeney, C., Tarasick, D.W., Thompson, A.M., Thouret, V., Witte, J.C., Wofsy, S.C., Ryerson, T.B., 2020. Global-scale distribution of ozone in the remote troposphere from the ATom and HIPPO airborne field missions. Atmos. Chem. Phys. 20, 10611–10635. https://doi.org/10.5194/acp-20-10611-2020.

Castellanos, P., Boersma, K.F., Torres, O., de Haan, J.F., 2015. OMI tropospheric NO2 air mass factors over South America: effects of biomass burning aerosols. Atmos. Meas. Tech. 8, 3831–3849. https://doi.org/10.5194/amt-8-3831-2015.

Cazorla, M., Wolfe, G.M., Bailey, S.A., Swanson, A.K., Arkinson, H.L., Hanisco, T.F., 2015. A new airborne laser-induced fluorescence instrument for in situ detection of formaldehyde throughout the troposphere and lower stratosphere. Atmos. Meas. Tech. 8, 541–552. https://doi.org/10.5194/amt-8-541-2015.

Chan Miller, C., Jacob, D.J., Marais, E.A., Yu, K., Travis, K.R., Kim, P.S., Fisher, J.A., Zhu, L., Wolfe, G.M., Hanisco, T.F., Keutsch, F.N., Kaiser, J., Min, K.E., Brown, S.S., Washenfelder, R.A., González Abad, G., Chance, K., 2017. Glyoxal yield from isoprene oxidation and relation to formaldehyde: chemical mechanism, constraints from SENEX aircraft observations, and interpretation of OMI satellite data. Atmos. Chem. Phys. 17, 8725–8738. https://doi.org/10.5194/acp-17-8725-2017.

Chance, K., 1998. Analysis of BrO measurements from the global ozone monitoring experiment. Geophys. Res. Lett. 25, 3335–3338. https://doi.org/10.1029/98GL52359.

Chance, K., Palmer, P.I., Spurr, R.J.D., Martin, R.V., Kurosu, T.P., Jacob, D.J., 2000. Satellite observations of formaldehyde over North America from GOME. Geophys. Res. Lett. 27, 3461–3464. https://doi.org/10.1029/2000GL011857.

Choi, J., Henze, D.K., Cao, H., Nowlan, C.R., González Abad, G., Kwon, H.-A., Lee, H.-M., Oak, Y.J., Park, R.J., Bates, K.H., Maasakkers, J.D., Wisthaler, A., Weinheimer, A.J., 2022. An inversion framework for optimizing non-methane VOC emissions using remote sensing and airborne observations in northeast Asia during the KORUS-AQ field campaign. J. Geophys. Res. 127. https://doi.org/10.1029/2021JD035844 e2021JD035844.

Curci, G., Palmer, P.I., Kurosu, T.P., Chance, K., Visconti, G., 2010. Estimating European volatile organic compound emissions using satellite observations of formaldehyde from the ozone monitoring instrument. Atmos. Chem. Phys. 10, 11501–11517. https://doi.org/10.5194/acp-10-11501-2010.

Dahlkötter, F., Gysel, M., Sauer, D., Minikin, A., Baumann, R., Seifert, P., Ansmann, A., Fromm, M., Voigt, C., Weinzierl, B., 2014. The pagami creek smoke plume after long-range transport to the upper troposphere over Europe – aerosol properties and Black carbon mixing state. Atmos. Chem. Phys. 14, 6111–6137. https://doi.org/10.5194/acp-14-6111-2014.

De Smedt, I., Stavrakou, T., Müller, J.-F., van der A, R.J., Van Roozendael, M., 2010. Trend detection in satellite observations of formaldehyde tropospheric columns. Geophys. Res. Lett. 37, L18808. https://doi.org/10.1029/2010GL044245.

De Smedt, I., Müller, J.F., Stavrakou, T., van der A, R., Eskes, H., Van Roozendael, M., 2008. Twelve years of global observations of formaldehyde in the troposphere using GOME and SCIAMACHY sensors. Atmos. Chem. Phys. 8, 4947–4963. https://doi.org/10.5194/acp-8-4947-2008.

De Smedt, I., Van Roozendael, M., Stavrakou, T., Müller, J.F., Lerot, C., Theys, N., Valks, P., Hao, N., van der A, R., 2012. Improved retrieval of global tropospheric formaldehyde columns from GOME-2/MetOp-A addressing noise reduction and instrumental degradation issues. Atmos. Meas. Tech. 5, 2933–2949. https://doi.org/10.5194/amt-5-2933-2012.

De Smedt, I., Stavrakou, T., Hendrick, F., Danckaert, T., Vlemmix, T., Pinardi, G., Theys, N., Lerot, C., Gielen, C., Vigouroux, C., Hermans, C., Fayt, C., Veefkind, P., Müller, J.F., Van Roozendael, M., 2015. Diurnal, seasonal and long-term variations of global formaldehyde columns inferred from combined OMI and GOME-2 observations. Atmos. Chem. Phys. 15, 12519–12545. https://doi.org/10.5194/acp-15-12519-2015.

De Smedt, I., Theys, N., Yu, H., Danckaert, T., Lerot, C., Compernolle, S., Van Roozendael, M., Richter, A., Hilboll, A., Peters, E., Pedergnana, M., Loyola, D., Beirle, S., Wagner, T., Eskes, H., van Geffen, J., Boersma, K.F., Veefkind, P., 2018. Algorithm theoretical baseline for formaldehyde retrievals from S5P TROPOMI and from the QA4ECV project. Atmos. Meas. Tech. 11, 2395–2426. https://doi.org/10.5194/amt-11-2395-2018.

De Smedt, I., Pinardi, G., Vigouroux, C., Compernolle, S., Bais, A., Benavent, N., Boersma, F., Chan, K.-L., Donner, S., Eichmann, K.-U., Hedelt, P., Hendrick, F., Irie, H., Kumar, V., Lambert, J.-C., Langerock, B., Lerot, C., Liu, C., Loyola, D., Piters, A., Richter, A., Rivera Cárdenas, C., Romahn, F., Ryan, R.G., Sinha, V., Theys, N., Vlietinck, J., Wagner, T., Wang, T., Yu, H., Van Roozendael, M., 2021. Comparative assessment of TROPOMI and OMI formaldehyde observations and validation against MAX-DOAS network column measurements. Atmos. Chem. Phys. 21, 12561–12593. https://doi.org/10.5194/acp-21-12561-2021.

Dubovik, O., Holben, B., Eck, T., Smirnov, A., Kaufman, Y., King, M., Tanré, D., Slutsker, I., 2002. Variability of absorption and optical properties of key aerosol types observed in worldwide locations. J. Atmos. Sci. 59, 590–608. https://doi.org/10.1175/1520-0469(2002)059<0590:VOAAOP>2.0.CO;2.

ESA, 2021. Sentinel-5 precursor calibration and validation plan for the operational phase. ref: ESA-EOPG-CSCOP-PL-0073, issue:1.1, available at: https://sentinel.esa.int/documents/247904/2474724/Sentinel-5P-Calibration-and-Validation-Plan.pdf. last access: 2022-11-11.

Fan, J., Ju, T., Wang, Q., Gao, H., Huang, R., Duan, J., 2021. Spatiotemporal variations and potential sources of tropospheric formaldehyde over eastern China based on OMI satellite data. Atmos. Pollut. Res. 12, 272–285. https://doi.org/10.1016/j.apr.2020.09.011.

Faulstich, S.D., Schissler, A.G., Strickland, M.J., Holmes, H.A., 2022. Statistical comparison and assessment of four fire emissions inventories for 2013 and a large wildfire in the Western United States. Fire 5, 27. https://doi.org/10.3390/fire5010027.

Ferreira, J., Reeves, C.E., Murphy, J.G., Garcia-Carreras, L., Parker, D.J., Oram, D.E., 2010. Isoprene emissions modelling for West Africa: MEGAN model evaluation and sensitivity analysis. Atmos. Chem. Phys. 10, 8453–8467. https://doi.org/10.5194/acp-10-8453-2010.

Franco, B., Hendrick, F., Van Roozendael, M., Müller, J.F., Stavrakou, T., Marais, E.A., Bovy, B., Bader, W., Fayt, C., Hermans, C., Lejeune, B., Pinardi, G., Servais, C., Mahieu, E., 2015. Retrievals of formaldehyde from ground-based FTIR and MAX-DOAS observations at the jungfraujoch station and comparisons with GEOS-chem and IMAGES model simulations. Atmos. Meas. Tech. 8, 1733–1756. https://doi.org/10.5194/amt-8-1733-2015.

Fried, A., Walega, J., Weibring, P., Richter, D., Simpson, I.J., Blake, D.R., Blake, N.J., Meinardi, S., Barletta, B., Hughes, S.C., Crawford, J.H., Diskin, G., Barrick, J., Hair, J., Fenn, M., Wisthaler, A., Mikoviny, T., Woo, J.-H., Park, M., Kim, J., Min, K.-E., Jeong, S., Wennberg, P.O., Kim, M.J., Crounse, J.D., Teng, A.P., Bennett, R., Yang-Martin, M., Shook, M.A., Huey, G., Tanner, D., Knote, C., Kim, J., Park, R., Brune, W., 2020. Airborne formaldehyde and volatile organic compound measurements over the daesan petrochemical complex on Korea's northwest Coast during the korea-united states air quality study: estimation of emission fluxes and effects on air quality. Elementa: Science of the Anthropocene 8, 121. https://doi.org/10.1525/elementa.2020.121.

Fu, T.-M., Jacob, D.J., Palmer, P.I., Chance, K., Wang, Y.X., Barletta, B., Blake, D.R., Stanton, J.C., Pilling, M.J., 2007. Space-based formaldehyde measurements as constraints on volatile organic compound emissions in east and south Asia and implications for ozone. J. Geophys. Res. 112, D06312. https://doi.org/10.1029/2006JD007853.

Fu, Y., Li, R., Huang, J., Bergeron, Y., Fu, Y., Wang, Y., Gao, Z., 2018. Satellite-observed impacts of wildfires on regional atmosphere composition and the shortwave radiative forcing: a multiple case study. J. Geophys. Res. Atmos. 123, 8326–8343. https://doi.org/10.1029/2017JD027927.

Gelaro, R., McCarty, W., Suárez, M.J., Todling, R., Molod, A., Takacs, L., Randles, C.A., Darmenov, A., Bosilovich, M.G., Reichle, R., Wargan, K., Coy, L., Cullather, R., Draper, C., Akella, S., Buchard, V., Conaty, A., da Silva, A.M., Gu, W., Kim, G.-K., Koster, R., Lucchesi, R., Merkova, D., Nielsen, J.E., Partyka, G., Pawson, S., Putman, W., Rienecker, M., Schubert, S.D., Sienkiewicz, M., Zhao, B., 2017. The modern-era retrospective analysis for research and applications, version 2 (MERRA-2). J. Clim. 30, 5419–5454. https://doi.org/10.1175/jcli-d-16-0758.1.

Giglio, L., Randerson, J.T., van der Werf, G.R., 2013. Analysis of daily, monthly, and annual burned area using the fourth-generation global fire emissions database (GFED4). J. Geophys. Res. Biogeosci. 118, 317–328. https://doi.org/10.1002/jgrg.20042.

Gilman, J.B., Lerner, B.M., Kuster, W.C., Goldan, P.D., Warneke, C., Veres, P.R., Roberts, J.M., de Gouw, J.A., Burling, I.R., Yokelson, R.J., 2015. Biomass burning emissions and potential air quality impacts of volatile organic compounds and other trace gases from fuels common in the US. Atmos. Chem. Phys. 15, 13915–13938. https://doi.org/10.5194/acp-15-13915-2015.

González Abad, G., Vasilkov, A., Seftor, C., Liu, X., Chance, K., 2016. Smithsonian astrophysical observatory ozone mapping and profiler suite (SAO OMPS) formaldehyde retrieval. Atmos. Meas. Tech. 9, 2797–2812. https://doi.org/10.5194/amt-9-2797-2016.

González Abad, G., Liu, X., Chance, K., Wang, H., Kurosu, T.P., Suleiman, R., 2015. Updated smithsonian astrophysical observatory ozone monitoring instrument (SAO OMI) formaldehyde retrieval. Atmos. Meas. Tech. 8, 19–32. https://doi.org/10.5194/amt-8-19-2015.

Gonzi, S., Palmer, P.I., Barkley, M.P., De Smedt, I., Van Roozendael, M., 2011. Biomass burning emission estimates inferred from satellite column measurements of HCHO: sensitivity to co-emitted aerosol and injection height. Geophys. Res. Lett. 38, L14807. https://doi.org/10.1029/2011GL047890.

Guenther, A.B., Jiang, X., Heald, C.L., Sakulyanontvittaya, T., Duhl, T., Emmons, L.K., Wang, X., 2012. The model of emissions of gases and aerosols from Nature version 2.1 (MEGAN2.1): an extended and updated framework for modeling biogenic emissions. Geosci. Model Dev. (GMD) 5, 1471–1492. https://doi.org/10.5194/gmd-5-1471-2012.

Hassinen, S., Balis, D., Bauer, H., Begoin, M., Delcloo, A., Eleftheratos, K., Gimeno Garcia, S., Granville, J., Grossi, M., Hao, N., Hedelt, P., Hendrick, F., Hess, M., Heue, K.P., Hovila, J., Jønch-Sørensen, H., Kalakoski, N., Kauppi, A., Kiemle, S., Kins, L., Koukouli, M.E., Kujanpää, J., Lambert, J.C., Lang, R., Lerot, C., Loyola, D., Pedergnana, M., Pinardi, G., Romahn, F., van Roozendael, M., Lutz, R., De Smedt, I., Stammes, P., Steinbrecht, W., Tamminen, J., Theys, N., Tilstra, L.G., Tuinder, O.N.E., Valks, P., Zerefos, C., Zimmer, W., Zyrichidou, I., 2016. Overview of the O3M SAF GOME-2 operational atmospheric composition and UV radiation data products and data availability. Atmos. Meas. Tech. 9, 383–407. https://doi.org/10.5194/amt-9-383-2016.

Hawbaker, T.J., Vanderhoof, M.K., Beal, Y.-J., Takacs, J.D., Schmidt, G.L., Falgout, J.T., Williams, B., Fairaux, N.M., Caldwell, M.K., Picotte, J.J., Howard, S.M., Stitt, S., Dwyer, J.L., 2017. Mapping burned areas using dense time-series of Landsat data. Remote Sens. Environ. 198, 504–522. https://doi.org/10.1016/j.rse.2017.06.027.

Hewson, W., Bösch, H., Barkley, M.P., De Smedt, I., 2013. Characterisation of GOME-2 formaldehyde retrieval sensitivity. Atmos. Meas. Tech. 6, 371–386. https://doi.org/10.5194/amt-6-371-2013.

Hoesly, R.M., Smith, S.J., Feng, L., Klimont, Z., Janssens-Maenhout, G., Pitkanen, T., Seibert, J.J., Vu, L., Andres, R.J., Bolt, R.M., Bond, T.C., Dawidowski, L., Kholod, N., Kurokawa, J.I., Li, M., Liu, L., Lu, Z., Moura, M.C.P., O'Rourke, P.R., Zhang, Q., 2018. Historical (1750–2014) anthropogenic emissions of reactive gases and aerosols from the Community emissions data system (CEDS). Geosci. Model Dev. (GMD) 11, 369–408. https://doi.org/10.5194/gmd-11-369-2018.

Huijnen, V., Williams, J., van Weele, M., van Noije, T., Krol, M., Dentener, F., Segers, A., Houweling, S., Peters, W., de Laat, J., Boersma, F., Bergamaschi, P., van Velthoven, P., Le Sager, P., Eskes, H., Alkemade, F., Scheele, R., Nédélec, P., Pátz, H.-W., 2010. The global chemistry transport model TM5: description and evaluation of the tropospheric chemistry version 3.0. Geosci. Model Dev. (GMD) 3, 445–473. https://doi.org/10.5194/gmd-3-445-2010.

Ingmann, P., Veihelmann, B., Langen, J., Lamarre, D., Stark, H., Courrèges-Lacoste, G.B., 2012. Requirements for the GMES atmosphere service and ESA's implementation concept: sentinels-4/-5 and -5p. Remote Sens. Environ. 120, 58–69. https://doi.org/10.1016/j.rse.2012.01.023.

Jin, L., Permar, W., Selimovic, V., Ketcherside, D., Yokelson, R.J., Hornbrook, R.S., Apel, E.C., Ku, I.T., Collett Jr., J.L., Sullivan, A.P., Jaffe, D.A., Pierce, J.R., Fried, A., Coggon, M.M., Gkatzelis, G.I., Warneke, C., Fischer, E.V., Hu, L., 2022. Constraining Emissions of Volatile Organic Compounds from Western US Wildfires with WE-CAN and FIREX-AQ Airborne Observations. EGUsphere, pp. 1–39. https://doi.org/10.5194/egusphere-2022-1107, 2022.

Juncosa Calahorrano, J.F., Lindaas, J., O'Dell, K., Palm, B.B., Peng, Q., Flocke, F., Pollack, I.B., Garofalo, L.A., Farmer, D.K., Pierce, J.R., Collett Jr., J.L., Weinheimer, A., Campos, T., Hornbrook, R.S., Hall, S.R., Ullmann, K., Pothier, M.A., Apel, E.C., Permar, W., Hu, L., Hills, A.J., Montzka, D., Tyndall, G., Thornton, J.A., Fischer, E.V., 2021. Daytime oxidized reactive nitrogen partitioning in Western U.S. wildfire smoke plumes. J. Geophys. Res. Atmos. 126. https://doi.org/10.1029/2020JD033484 e2020JD033484.

June, N.A., Hodshire, A.L., Wiggins, E.B., Winstead, E.L., Robinson, C.E., Thornhill, K.L., Sanchez, K.J., Moore, R.H., Pagonis, D., Guo, H., Campuzano-Jost, P., Jimenez, J.L., Coggon, M.M., Dean-Day, J.M., Bui, T.P., Peischl, J., Yokelson, R.J., Alvarado, M.J., Kreidenweis, S.M., Jathar, S.H., Pierce, J.R., 2022. Aerosol size distribution changes in FIREX-AQ biomass burning plumes: the impact of plume concentration on coagulation and OA condensation/evaporation. Atmos. Chem. Phys. Discuss. 1–35. https://doi.org/10.5194/acp-2022-349, 2022.

Jung, J., Choi, Y., Mousavinezhad, S., Kang, D., Park, J., Pouyaei, A., Ghahremanloo, M., Momeni, M., Kim, H., 2022. Changes in the ozone chemical regime over the contiguous United States inferred by the inversion of NOx and VOC emissions using satellite observation. Atmos. Res. 270, 106076. https://doi.org/10.1016/j.atmosres.2022.106076.

Jung, Y., González Abad, G., Nowlan, C.R., Chance, K., Liu, X., Torres, O., Ahn, C., 2019. Explicit aerosol correction of OMI formaldehyde retrievals. Earth Space Sci. 6, 2087–2105. https://doi.org/10.1029/2019EA000702.

Junghenn Noyes, K.T., Kahn, R.A., Limbacher, J.A., Li, Z., Fenn, M.A., Giles, D.M., Hair, J.W., Katich, J.M., Moore, R.H., Robinson, C.E., Sanchez, K.J., Shingler, T.J., Thornhill, K.L., Wiggins, E.B., Winstead, E.L., 2020. Wildfire smoke particle

properties and evolution, from space-based multi-angle imaging II: the williams flats fire during the FIREX-AQ campaign. Remote Sens. 12, 3823. https://doi.org/10.3390/rs12223823.

Kaiser, J.W., Heil, A., Andreae, M.O., Benedetti, A., Chubarova, N., Jones, L., Morcrette, J.J., Razinger, M., Schultz, M.G., Suttie, M., van der Werf, G.R., 2012. Biomass burning emissions estimated with a global fire assimilation system based on observed fire radiative power. Biogeosciences 9, 527–554. https://doi.org/10.5194/bg-9-527-2012.

Kesselmeier, J., Kuhn, U., Rottenberger, S., Biesenthal, T., Wolf, A., Schebeske, G., Andreae, M.O., Ciccioli, P., Brancaleoni, E., Frattoni, M., Oliva, S.T., Botelho, M.L., Silva, C.M.A., Tavares, T.M., 2002. Concentrations and species composition of atmospheric volatile organic compounds (VOCs) as observed during the wet and dry season in Rondônia (amazonia). J. Geophys. Res. 107, 8053. https://doi.org/10.1029/2000JD000267.

Khokhar, M.F., Frankenberg, C., Van Roozendael, M., Beirle, S., Kühl, S., Richter, A., Platt, U., Wagner, T., 2005. Satellite observations of atmospheric SO2 from volcanic eruptions during the time-period of 1996–2002. Adv. Space Res. 36, 879–887. https://doi.org/10.1016/j.asr.2005.04.114.

Kim, J.H., Kim, S.M., Baek, K.H., Wang, L., Kurosu, T., De Smedt, I., Chance, K., Newchurch, M.J., 2011. Evaluation of satellite-derived HCHO using statistical methods. Atmos. Chem. Phys. Discuss. 8003–8025. https://doi.org/10.5194/acpd-11-8003-2011, 2011.

Kim, J., Jeong, U., Ahn, M.-H., Kim, J.H., Park, R.J., Lee, H., Song, C.H., Choi, Y.-S., Lee, K.-H., Yoo, J.-M., Jeong, M.-J., Park, S.K., Lee, K.-M., Song, C.-K., Kim, S.-W., Kim, Y.J., Kim, S.-W., Kim, M., Go, S., Liu, X., Chance, K., Chan Miller, C., Al-Saadi, J., Veihelmann, B., Bhartia, P.K., Torres, O., Abad, G.G., Haffner, D.P., Ko, D. H., Lee, S.H., Woo, J.-H., Chong, H., Park, S.S., Nicks, D., Choi, W.J., Moon, K.-J., Cho, A., Yoon, J., Kim, S.-k., Hong, H., Lee, K., Lee, H., Lee, S., Choi, M., Veefkind, P., Levelt, P.F., Edwards, D.P., Kang, M., Eo, M., Bak, J., Baek, K., Kwon, H.-A., Yang, J., Park, J., Han, K.M., Kim, B.-R., Shin, H.-W., Choi, H., Lee, E., Chong, J., Cha, Y., Koo, J.-H., Irie, H., Hayashida, S., Kasai, Y., Kanaya, Y., Liu, C., Lin, J., Crawford, J. H., Carmichael, G.R., Newchurch, M.J., Lefer, B.L., Herman, J.R., Swap, R.J., Lau, A. K.H., Kurosu, T.P., Jaross, G., Ahlers, B., Dobber, M., McElroy, C.T., Choi, Y., 2020. New era of air quality monitoring from space: geostationary environment monitoring spectrometer (GEMS). B. Am. Meteorol. Soc. 101, E1–E22. https://doi.org/10.1175/bams-d-18-0013.1.

Kunzli, N., Avol, E., Wu, J., Gauderman, W.J., Rappaport, E., Millstein, J., Bennion, J., McConnell, R., Gilliland, F.D., Berhane, K., Lurmann, F., Winer, A., Peters, J.M., 2006. Health effects of the 2003 southern California wildfires on children. Am. J. Respir. Crit. Care Med. 174, 1221–1228. https://doi.org/10.1164/rccm.200604-519OC.

Kwon, H.-A., Park, R.J., Jeong, J.I., Lee, S., González Abad, G., Kurosu, T.P., Palmer, P.I., Chance, K., 2017. Sensitivity of formaldehyde (HCHO) column measurements from a geostationary satellite to temporal variation of the air mass factor in east Asia. Atmos. Chem. Phys. 17, 4673–4686. https://doi.org/10.5194/acp-17-4673-2017.

Kwon, H.-A., Park, R.J., González Abad, G., Chance, K., Kurosu, T.P., Kim, J., De Smedt, I., Van Roozendael, M., Peters, E., Burrows, J., 2019. Description of a formaldehyde retrieval algorithm for the geostationary environment monitoring spectrometer (GEMS). Atmos. Meas. Tech. 12, 3551–3571. https://doi.org/10.5194/amt-12-3551-2019.

Leitão, J., Richter, A., Vrekoussis, M., Kokhanovsky, A., Zhang, Q.J., Beekmann, M., Burrows, J.P., 2010. On the improvement of NO2 satellite retrievals – aerosol impact on the airmass factors. Atmos. Meas. Tech. 3, 475–493. https://doi.org/10.5194/amt-3-475-2010.

Levelt, P.F., Stein Zweers, D.C., Aben, I., Bauwens, M., Borsdorff, T., De Smedt, I., Eskes, H.J., Lerot, C., Loyola, D.G., Romahn, F., Stavrakou, T., Theys, N., Van Roozendael, M., Veefkind, J.P., Verhoelst, T., 2022. Air quality impacts of COVID-19 lockdown measures detected from space using high spatial resolution observations of multiple trace gases from Sentinel-5P/TROPOMI. Atmos. Chem. Phys. 22, 10319–10351. https://doi.org/10.5194/acp-22-10319-2022.

Li, C., Joiner, J., Krotkov, N.A., Dunlap, L., 2015. A new method for global retrievals of HCHO total columns from the suomi national Polar-orbiting partnership ozone mapping and profiler suite. Geophys. Res. Lett. 42, 2515–2522. https://doi.org/10.1002/2015GL063204.

Li, J., Zhang, M., Tao, J., Han, X., Xu, Y., 2022. OMI formaldehyde column constrained emissions of reactive volatile organic compounds over the pearl river Delta region of China. Sci. Total Environ. 826, 154121. https://doi.org/10.1016/j.scitotenv.2022.154121.

Liang, Y., Weber, R.J., Misztal, P.K., Jen, C.N., Goldstein, A.H., 2022. Aging of volatile organic compounds in October 2017 northern California wildfire plumes. Environ. Sci. Technol. 56, 1557–1567. https://doi.org/10.1021/acs.est.1c05684.

Liao, J., Hanisco, T.F., Wolfe, G.M., St Clair, J., Jimenez, J.L., Campuzano-Jost, P., Nault, B.A., Fried, A., Marais, E.A., Gonzalez Abad, G., Chance, K., Jethva, H.T., Ryerson, T.B., Warneke, C., Wisthaler, A., 2019. Towards a satellite formaldehyde – in situ hybrid estimate for organic aerosol abundance. Atmos. Chem. Phys. 19, 2765–2785. https://doi.org/10.5194/acp-19-2765-2019.

Liao, J., Wolfe, G.M., Hannun, R.A., St Clair, J.M., Hanisco, T.F., Gilman, J.B., Lamplugh, A., Selimovic, V., Diskin, G.S., Nowak, J.B., Halliday, H.S., DiGangi, J.P., Hall, S.R., Ullmann, K., Holmes, C.D., Fite, C.H., Agastra, A., Ryerson, T.B., Peischl, J., Bourgeois, I., Warneke, C., Coggon, M.M., Gkatzelis, G.I., Sekimoto, K., Fried, A., Richter, D., Weibring, P., Apel, E.C., Hornbrook, R.S., Brown, S.S., Womack, C.C., Robinson, M.A., Washenfelder, R.A., Veres, P.R., Neuman, J.A., 2021. Formaldehyde evolution in US wildfire plumes during the fire influence on regional to global environments and air quality experiment (FIREX-AQ). Atmos. Chem. Phys. 21, 18319–18331. https://doi.org/10.5194/acp-21-18319-2021.

Lieschke, K.J., Fisher, J.A., Paton-Walsh, C., Jones, N.B., Greenslade, J.W., Burden, S., Griffith, D.W.T., 2019. Decreasing trend in formaldehyde detected from 20-Year record at Wollongong, southeast Australia. Geophys. Res. Lett. 46, 8464–8473. https://doi.org/10.1029/2019GL083757.

Lill, E., Lindaas, J., Juncosa Calahorrano, J.F., Campos, T., Flocke, F., Apel, E.C., Hornbrook, R.S., Hills, A., Jarnot, A., Blake, N., Permar, W., Hu, L., Weinheimer, A., Tyndall, G., Montzka, D.D.e., Hall, S.R., Ullmann, K., Thornton, J., Palm, B.B., Peng, Q., Pollack, I., Fischer, E.V., 2022. Wildfire-driven changes in the abundance of gas-phase pollutants in the city of Boise, ID during summer 2018. Atmos. Pollut. Res. 13, 101269. https://doi.org/10.1016/j.apr.2021.101269.

Lindaas, J., Pollack, I.B., Garofalo, L.A., Pothier, M.A., Farmer, D.K., Kreidenweis, S.M., Campos, T.L., Flocke, F., Weinheimer, A.J., Montzka, D.D., Tyndall, G.S., Palm, B.B., Peng, Q., Thornton, J.A., Permar, W., Wielgasz, C., Hu, L., Ottmar, R.D., Restaino, J. C., Hudak, A.T., Ku, I.-T., Zhou, Y., Sive, B.C., Sullivan, A., Collett Jr., J.L., Fischer, E. V., 2021. Emissions of reactive nitrogen from Western U.S. wildfires during summer 2018. J. Geophys. Res. Atmos. 126. https://doi.org/10.1029/2020JD032657, 2020JD032657.

Liu, R., Feng, T., Wang, S., Shi, C., Guo, Y., Nan, J., Deng, Y., Zhou, B., 2018. OMI satellite observed formaldehyde column from 2006 to 2015 over xishuangbanna, southwest China, and validation using ground based zenith-sky DOAS. Sci. Total Environ. 613–614, 168–175. https://doi.org/10.1016/j.scitotenv.2017.08.210.

Lorente, A., Folkert Boersma, K., Yu, H., Dörner, S., Hilboll, A., Richter, A., Liu, M., Lamsal, L.N., Barkley, M., De Smedt, I., Van Roozendael, M., Wang, Y., Wagner, T., Beirle, S., Lin, J.T., Krotkov, N., Stammes, P., Wang, P., Eskes, H.J., Krol, M., 2017. Structural uncertainty in air mass factor calculation for NO2 and HCHO satellite retrievals. Atmos. Meas. Tech. 10, 759–782. https://doi.org/10.5194/amt-10-759-2017.

Marais, E.A., Jacob, D.J., Kurosu, T.P., Chance, K., Murphy, J.G., Reeves, C., Mills, G., Casadio, S., Millet, D.B., Barkley, M.P., Paulot, F., Mao, J., 2012. Isoprene emissions in Africa inferred from OMI observations of formaldehyde columns. Atmos. Chem. Phys. 12, 6219–6235. https://doi.org/10.5194/acp-12-6219-2012.

Marbach, T., Beirle, S., Liu, C., Platt, U., Wagner, T., 2008. Biomass burning emissions from satellite observations: synergistic use of formaldehyde (HCHO), fire counts, and surface temperature. In: Remote Sensing of Fire: Science and Application. Proc., vol 7089. SPIE, p. 7089. https://doi.org/10.1117/12.793654, 2008.

Martin, R.V., Parrish, D.D., Ryerson, T.B., Nicks Jr., D.K., Chance, K., Kurosu, T.P., Jacob, D.J., Sturges, E.D., Fried, A., Wert, B.P., 2004. Evaluation of GOME satellite measurements of tropospheric NO2 and HCHO using regional data from aircraft campaigns in the southeastern United States. J. Geophys. Res. 109, D24307. https://doi.org/10.1029/2004JD004869.

Millet, D.B., Jacob, D.J., Boersma, K.F., Fu, T.-M., Kurosu, T.P., Chance, K., Heald, C.L., Guenther, A., 2008. Spatial distribution of isoprene emissions from North America derived from formaldehyde column measurements by the OMI satellite sensor. J. Geophys. Res. 113, D02307. https://doi.org/10.1029/2007JD008950.

Millet, D.B., Jacob, D.J., Turquety, S., Hudman, R.C., Wu, S., Fried, A., Walega, J., Heikes, B.G., Blake, D.R., Singh, H.B., Anderson, B.E., Clarke, A.D., 2006. Formaldehyde distribution over North America: implications for satellite retrievals of formaldehyde columns and isoprene emission. J. Geophys. Res. 111, D24S02. https://doi.org/10.1029/2005JD006853.

Nowlan, C.R., González Abad, G., Kwon, H.-A., Ayazpour, Z., Chan Miller, C., Chance, K., Chong, H., Liu, X., O'Sullivan, E., Wang, H., Zhu, L., De Smedt, I., Jaross, G., Seftor, C., Sun, K., 2023. Global formaldehyde products from the ozone mapping and profiler suite (OMPS) nadir mappers on suomi NPP and NOAA-20. Earth Space Sci. https://doi.org/10.1029/2022EA002643.

Palm, B.B., Peng, Q., Hall, S.R., Ullmann, K., Campos, T.L., Weinheimer, A., Montzka, D., Tyndall, G., Permar, W., Hu, L., Flocke, F., Fischer, E.V., Thornton, J.A., 2021. Spatially resolved photochemistry impacts emissions estimates in fresh wildfire plumes. Geophys. Res. Lett. 48. https://doi.org/10.1029/2021GL095443 e2021GL095443.

Palmer, P.I., Jacob, D.J., Fiore, A.M., Martin, R.V., Chance, K., Kurosu, T.P., 2003. Mapping isoprene emissions over North America using formaldehyde column observations from space. J. Geophys. Res. 108. https://doi.org/10.1029/2002JD002153.

Palmer, P.I., Jacob, D.J., Chance, K., Martin, R.V., Spurr, R.J.D., Kurosu, T.P., Bey, I., Yantosca, R., Fiore, A., Li, Q., 2001. Air mass factor formulation for spectroscopic measurements from satellites: application to formaldehyde retrievals from the global ozone monitoring experiment. J. Geophys. Res. 106, 14539–14550. https://doi.org/10.1029/2000jd900772.

Permar, W., Jin, L., Peng, Q., O'Dell, K., Lill, E., Selimovic, V., Yokelson, R.J., Hornbrook, R.S., Hills, A.J., Apel, E.C., Ku, I.T., Zhou, Y., Sive, B.C., Sullivan, A.P., Collett, J.L., Palm, B.B., Thornton, J.A., Flocke, F., Fischer, E.V., Hu, L., 2023. Atmospheric OH reactivity in the western United States determined from comprehensive gas-phase measurements during WE-CAN. Environ. Sci.: Atmos. 3, 97–114. https://doi.org/10.1039/D2EA00063F.

Permar, W., Wang, Q., Selimovic, V., Wielgasz, C., Yokelson, R.J., Hornbrook, R.S., Hills, A.J., Apel, E.C., Ku, I.-T., Zhou, Y., Sive, B.C., Sullivan, A.P., Collett Jr., J.L., Campos, T.L., Palm, B.B., Peng, Q., Thornton, J.A., Garofalo, L.A., Farmer, D.K., Kreidenweis, S.M., Levin, E.J.T., DeMott, P.J., Flocke, F., Fischer, E.V., Hu, L., 2021. Emissions of trace organic gases from Western U.S. wildfires based on WE-CAN aircraft measurements. J. Geophys. Res. 126. https://doi.org/10.1029/2020JD033838 e2020JD033838.

Peters, E., Wittrock, F., Großmann, K., Frieß, U., Richter, A., Burrows, J.P., 2012. Formaldehyde and nitrogen dioxide over the remote western Pacific Ocean: SCIAMACHY and GOME-2 validation using ship-based MAX-DOAS observations. Atmos. Chem. Phys. 12, 11179–11197. https://doi.org/10.5194/acp-12-11179-2012.

Pu, D., Zhu, L., De Smedt, I., Li, X., Sun, W., Wang, D., Liu, S., Li, J., Shu, L., Chen, Y., Sun, S., Zuo, X., Fu, W., Xu, P., Yang, X., Fu, T.-M., 2022. Response of anthropogenic volatile organic compound emissions to urbanization in Asia probed with TROPOMI and VIIRS satellite observations. Geophys. Res. Lett. 49. https://doi.org/10.1029/2022GL099470 e2022GL099470.

Rémy, S., Veira, A., Paugam, R., Sofiev, M., Kaiser, J.W., Marenco, F., Burton, S.P., Benedetti, A., Engelen, R.J., Ferrare, R., Hair, J.W., 2017. Two global data sets of daily fire emission injection heights since 2003. Atmos. Chem. Phys. 17, 2921–2942. https://doi.org/10.5194/acp-17-2921-2017.

Richter, D., Weibring, P., Walega, J.G., Fried, A., Spuler, S.M., Taubman, M.S., 2015. Compact highly sensitive multi-species airborne mid-IR spectrometer. Appl. Phys. B 119, 119–131. https://doi.org/10.1007/s00340-015-6038-8.

Ridley, B.A., Grahek, F.E., Small, A., Flow, Low, 1990. High sensitivity reaction vessel for NO chemiluminescence detectors. J. Atmos. Ocean. Technol. 7, 307–311. https://doi.org/10.1175/1520-0426(1990)007<0307:ASLFHS>2.0.CO;2.

Ridley, B.A., Grahek, F.E., Walega, J.G., 1992. A small High-sensitivity, medium-response ozone detector suitable for measurements from light aircraft. J. Atmos. Ocean. Technol. 9, 142–148. https://doi.org/10.1175/1520-0426(1992)009<0142:ASHSMR>2.0.CO;2.

Sachse, G.W., Collins Jr., J.E., Hill, G.F., Wade, L.O., Burney, L.G., Ritter, J.A., 1991. Airborne tunable diode laser sensor for high-precision concentration and flux measurements of carbon monoxide and methane. Meas. Atmos. Gases 1433, 157. https://doi.org/10.1117/12.46162.

Shen, L., Jacob, D.J., Zhu, L., Zhang, Q., Zheng, B., Sulprizio, M.P., Li, K., De Smedt, I., González Abad, G., Cao, H., Fu, T.-M., Liao, H., 2019. The 2005–2016 trends of formaldehyde columns over China observed by satellites: increasing anthropogenic emissions of volatile organic compounds and decreasing agricultural fire emissions. Geophys. Res. Lett. 46, 4468–4475. https://doi.org/10.1029/2019GL082172.

Singh, H.B., Brune, W.H., Crawford, J.H., Flocke, F., Jacob, D.J., 2009. Chemistry and transport of pollution over the Gulf of Mexico and the Pacific: spring 2006 INTEX-B campaign overview and first results. Atmos. Chem. Phys. 9, 2301–2318. https://doi.org/10.5194/acp-9-2301-2009.

Sitnov, S.A., Mokhov, I.I., 2017. Formaldehyde and nitrogen dioxide in the atmosphere during summer weather extremes and wildfires in european Russia in 2010 and Western siberia in 2012. Int. J. Rem. Sens. 38, 4086–4106. https://doi.org/10.1080/01431161.2017.1312618.

Souri, A.H., Nowlan, C.R., González Abad, G., Zhu, L., Blake, D.R., Fried, A., Weinheimer, A.J., Wisthaler, A., Woo, J.H., Zhang, Q., Chan Miller, C.E., Liu, X., Chance, K., 2020. An inversion of NOx and non-methane volatile organic compound (NMVOC) emissions using satellite observations during the KORUS-AQ campaign and implications for surface ozone over east Asia. Atmos. Chem. Phys. 20, 9837–9854. https://doi.org/10.5194/acp-20-9837-2020.

Su, W., Liu, C., Hu, Q., Zhao, S., Sun, Y., Wang, W., Zhu, Y., Liu, J., Kim, J., 2019. Primary and secondary sources of ambient formaldehyde in the yangtze river Delta based on ozone mapping and profiler suite (OMPS) observations. Atmos. Chem. Phys. 19, 6717–6736. https://doi.org/10.5194/acp-19-6717-2019.

Su, W., Liu, C., Chan, K.L., Hu, Q., Liu, H., Ji, X., Zhu, Y., Liu, T., Zhang, C., Chen, Y., Liu, J., 2020. An improved TROPOMI tropospheric HCHO retrieval over China. Atmos. Meas. Tech. 13, 6271–6292. https://doi.org/10.5194/amt-13-6271-2020.

Su, W., Hu, Q., Chen, Y., Lin, J., Zhang, C., Liu, C., 2022. Inferring global surface HCHO concentrations from multisource hyperspectral satellites and their application to HCHO-Related global cancer burden estimation. Environ. Int. 170, 107600. https://doi.org/10.1016/j.envint.2022.107600.

Sun, W., Zhu, L., De Smedt, I., Bai, B., Pu, D., Chen, Y., Shu, L., Wang, D., Fu, T.-M., Wang, X., Yang, X., 2021. Global significant changes in formaldehyde (HCHO) columns observed from space at the early stage of the COVID-19 pandemic. Geophys. Res. Lett. 48. https://doi.org/10.1029/2020GL091265, 2e020GL091265.

Veefkind, J.P., Boersma, K.F., Wang, J., Kurosu, T.P., Krotkov, N., Chance, K., Levelt, P. F., 2011. Global satellite analysis of the relation between aerosols and short-lived trace gases. Atmos. Chem. Phys. 11, 1255–1267. https://doi.org/10.5194/acp-11-1255-2011.

Vigouroux, C., Langerock, B., Bauer Aquino, C.A., Blumenstock, T., Cheng, Z., De Mazière, M., De Smedt, I., Grutter, M., Hannigan, J.W., Jones, N., Kivi, R., Loyola, D., Lutsch, E., Mahieu, E., Makarova, M., Metzger, J.-M., Morino, I., Murata, I., Nagahama, T., Notholt, J., Ortega, I., Palm, M., Pinardi, G., Röhling, A., Smale, D., Stremme, W., Strong, K., Sussmann, R., Té, Y., van Roozendael, M., Wang, P., Winkler, H., 2020. TROPOMI–Sentinel-5 precursor formaldehyde validation using an extensive network of ground-based Fourier-transform infrared stations. Atmos. Meas. Tech. 13, 3751–3767. https://doi.org/10.5194/amt-13-3751-2020.

Wang, P., Holloway, T., Bindl, M., Harkey, M., De Smedt, I., 2022. Ambient formaldehyde over the United States from ground-based (AQS) and satellite (OMI) observations. Remote Sens. 14, 2191. https://doi.org/10.3390/rs14092191.

Wang, Y., Beirle, S., Lampel, J., Koukouli, M., De Smedt, I., Theys, N., Li, A., Wu, D., Xie, P., Liu, C., Van Roozendael, M., Stavrakou, T., Müller, J.-F., Wagner, T., 2017. Validation of OMI, GOME-2A and GOME-2B tropospheric NO_2, SO_2 and HCHO products using MAX-DOAS observations from 2011 to 2014 in wuxi, China: investigation of the effects of priori profiles and aerosols on the satellite products. Atmos. Chem. Phys. 17, 5007–5033. https://doi.org/10.5194/acp-17-5007-2017.

Warneke, C., Schwarz, J.P., Dibb, J., Kalashnikova, O., Frost, G., Al-Saadi, J., Brown, S.S., Brewer, W.A., Soja, A., Seidel, F.C., Washenfelder, R.A., Wiggins, E.B., Moore, R.H., Anderson, B.E., Jordan, C., Yacovitch, T.I., Herndon, S.C., Liu, S., Kuwayama, T., Jaffe, D., Johnston, N., Selimovic, V., Yokelson, R., Giles, D.M., Holben, B.N., Goloub, P., Popovici, I., Trainer, M., Kumar, A., Pierce, R.B., Fahey, D., Roberts, J., Gargulinski, E.M., Peterson, D.A., Ye, X., Thapa, L.H., Saide, P.E., Fite, C.H., Holmes, C.D., Wang, S., Coggon, M.M., Decker, Z.C.J., Stockwell, C.E., Xu, L., Gkatzelis, G., Aikin, K., Lefer, B., Kaspari, J., Griffin, D., Zeng, L., Weber, R., Hastings, M., Chai, J., Wolfe, G.M., Hanisco, T.F., Liao, J., Jost, P.C., Guo, H., Jimenez, J.L., Crawford, J., 2022. Fire influence on regional to global environments and air quality (FIREX-AQ). J. Geophys. Res. 128. https://doi.org/10.1029/2022JD037758 e2022JD037758.

Williams, J.E., Boersma, K.F., Le Sager, P., Verstraeten, W.W., 2017. The high-resolution version of TM5-MP for optimized satellite retrievals: description and validation. Geosci. Model Dev. (GMD) 10, 721–750. https://doi.org/10.5194/gmd-10-721-2017.

Wittrock, F., Richter, A., Oetjen, H., Burrows, J.P., Kanakidou, M., Myriokefalitakis, S., Volkamer, R., Beirle, S., Platt, U., Wagner, T., 2006. Simultaneous global observations of glyoxal and formaldehyde from space. Geophys. Res. Lett. 33. https://doi.org/10.1029/2006gl026310.

Wolfe, G.M., Nicely, J.M., St Clair, J.M., Hanisco, T.F., Liao, J., Oman, L.D., Brune, W.B., Miller, D., Thames, A., González Abad, G., Ryerson, T.B., Thompson, C.R., Peischl, J., McKain, K., Sweeney, C., Wennberg, P.O., Kim, M., Crounse, J.D., Hall, S.R., Ullmann, K., Diskin, G., Bui, P., Chang, C., Dean-Day, J., 2019. Mapping hydroxyl variability throughout the global remote troposphere via synthesis of airborne and satellite formaldehyde observations. Proc. Natl. Acad. Sci. U. S. A 116, 11171–11180. https://doi.org/10.1073/pnas.1821661116.

Wolfe, G.M., Hanisco, T.F., Arkinson, H.L., Blake, D.R., Wisthaler, A., Mikoviny, T., Ryerson, T.B., Pollack, I., Peischl, J., Wennberg, P.O., Crounse, J.D., St Clair, J.M., Teng, A., Huey, L.G., Liu, X., Fried, A., Weibring, P., Richter, D., Walega, J., Hall, S. R., Ullmann, K., Jimenez, J.L., Campuzano-Jost, P., Bui, T.P., Diskin, G., Podolske, J. R., Sachse, G., Cohen, R.C., 2022. Photochemical evolution of the 2013 California rim fire: synergistic impacts of reactive hydrocarbons and enhanced oxidants. Atmos. Chem. Phys. 22, 4253–4275. https://doi.org/10.5194/acp-22-4253-2022.

Xu, L., Crounse, J.D., Vasquez, K.T., Allen, H., Wennberg, P.O., Bourgeois, I., Brown, S.S., Campuzano-Jost, P., Coggon, M.M., Crawford, J.H., DiGangi, J.P., Diskin, G.S., Fried, A., Gargulinski, E.M., Gilman, J.B., Gkatzelis, G.I., Guo, H., Hair, J.W., Hall, S. R., Halliday, H.A., Hanisco, T.F., Hannun, R.A., Holmes, C.D., Huey, L.G., Jimenez, J. L., Lamplugh, A., Lee, Y.R., Liao, J., Lindaas, J., Neuman, J.A., Nowak, J.B., Peischl, J., Peterson, D.A., Piel, F., Richter, D., Rickly, P.S., Robinson, M.A., Rollins, A.W., Ryerson, T.B., Sekimoto, K., Selimovic, V., Shingler, T., Soja, A.J., St Clair, J.M., Tanner, D.J., Ullmann, K., Veres, P.R., Walega, J., Warneke, C., Washenfelder, R.A., Weibring, P., Wisthaler, A., Wolfe, G.M., Womack, C.C., Yokelson, R.J., 2021. Ozone chemistry in western U.S. wildfire plumes. Sci. Adv. 7. https://doi.org/10.1126/sciadv.abl3648 eabl3648.

Xu, Q., Westerling, A.L., Notohamiprodjo, A., Wiedinmyer, C., Picotte, J.J., Parks, S.A., Hurteau, M.D., Marlier, M.E., Kolden, C.A., Sam, J.A., Baldwin, W.J., Ade, C., 2022. Wildfire burn severity and emissions inventory: an example implementation over California. Environ. Res. Lett. 17, 085008. https://doi.org/10.1088/1748-9326/ac80d0.

Yamasoe, M.A., Sauvage, B., Thouret, V., Nédélec, P., Le Flochmoen, E., Barret, B., 2015. Analysis of tropospheric ozone and carbon monoxide profiles over South America based on MOZAIC/IAGOS database and model simulations. Tellus B 67, 27884. https://doi.org/10.3402/tellusb.v67.27884.

Yokelson, R.J., Urbanski, S.P., Atlas, E.L., Toohey, D.W., Alvarado, E.C., Crounse, J.D., Wennberg, P.O., Fisher, M.E., Wold, C.E., Campos, T.L., Adachi, K., Buseck, P.R., Hao, W.M., 2007. Emissions from forest fires near Mexico City. Atmos. Chem. Phys. 7, 5569–5584. https://doi.org/10.5194/acp-7-5569-2007.

Zara, M., Boersma, K.F., De Smedt, I., Richter, A., Peters, E., van Geffen, J.H.G.M., Beirle, S., Wagner, T., Van Roozendael, M., Marchenko, S., Lamsal, L.N., Eskes, H.J., 2018. Improved slant column density retrieval of nitrogen dioxide and formaldehyde for OMI and GOME-2A from QA4ECV: Intercomparison, uncertainty characterisation, and trends. Atmos. Meas. Tech. 11, 4033–4058. https://doi.org/10.5194/amt-11-4033-2018.

Zeng, T., Liu, Z., Wang, Y., 2016. Large fire emissions in summer over the southeastern US: satellite measurements and modeling analysis. Atmos. Environ. 127, 213–220. https://doi.org/10.1016/j.atmosenv.2015.12.025.

Zhang, T., de Jong, M.C., Wooster, M.J., Xu, W., Wang, L., 2020. Trends in eastern China agricultural fire emissions derived from a combination of geostationary (Himawari) and polar (VIIRS) orbiter fire radiative power products. Atmos. Chem. Phys. 20, 10687–10705. https://doi.org/10.5194/acp-20-10687-2020.

Zhang, Y., Li, R., Min, Q., Bo, H., Fu, Y., Wang, Y., Gao, Z., 2019. The controlling factors of atmospheric formaldehyde (HCHO) in Amazon as seen from satellite. Earth Space Sci. 6, 959–971. https://doi.org/10.1029/2019EA000627.

Zhao, T., Mao, J., Simpson, W.R., De Smedt, I., Zhu, L., Hanisco, T.F., Wolfe, G.M., St Clair, J.M., González Abad, G., Nowlan, C.R., Barletta, B., Meinardi, S., Blake, D.R., Apel, E.C., Hornbrook, R.S., 2022. Source and variability of formaldehyde (HCHO) at northern high latitudes: an integrated satellite, aircraft, and model study. Atmos. Chem. Phys. 22, 7163–7178. https://doi.org/10.5194/acp-22-7163-2022.

Zhao, Y., Li, J., Wang, H., Gong, D., Li, Q., Wang, D., Wang, J., Wang, B., 2025. Enhanced validation and application of satellite-derived formaldehyde data for assessing photochemical pollution in the Chinese Greater Bay area. Environ. Pollut. 366, 125553. https://doi.org/10.1016/j.envpol.2024.125553.

Zhu, L., Mickley, L.J., Jacob, D.J., Marais, E.A., Sheng, J., Hu, L., Gonzaïlez Abad, G., Chance, K., 2017a. Long-term (2005–2014) trends in formaldehyde (HCHO) columns across North America as seen by the OMI satellite instrument: evidence of changing emissions of volatile organic compounds. Geophys. Res. Lett. 44, 7079–7086. https://doi.org/10.1002/2017GL073859.

Zhu, L., Jacob, D.J., Keutsch, F.N., Mickley, L.J., Scheffe, R., Strum, M., González Abad, G., Chance, K., Yang, K., Rappenglück, B., Millet, D.B., Baasandorj, M., Jaeglé, L., Shah, V., 2017b. Formaldehyde (HCHO) as a hazardous air pollutant: mapping surface air concentrations from satellite and inferring cancer risks in the United States. Environ. Sci. Technol. 51, 5650–5657. https://doi.org/10.1021/acs.est.7b01356.

Zhu, L., Jacob, D.J., Eastham, S.D., Sulprizio, M.P., Wang, X., Sherwen, T., Evans, M.J., Chen, Q., Alexander, B., Koenig, T.K., Volkamer, R., Huey, L.G., Le Breton, M., Bannan, T.J., Percival, C.J., 2019. Effect of sea salt aerosol on tropospheric bromine chemistry. Atmos. Chem. Phys. 19, 6497–6507. https://doi.org/10.5194/acp-19-6497-2019.

Zhu, L., González Abad, G., Nowlan, C.R., Chan Miller, C., Chance, K., Apel, E.C., DiGangi, J.P., Fried, A., Hanisco, T.F., Hornbrook, R.S., Hu, L., Kaiser, J., Keutsch, F. N., Permar, W., St Clair, J.M., Wolfe, G.M., 2020. Validation of satellite formaldehyde (HCHO) retrievals using observations from 12 aircraft campaigns. Atmos. Chem. Phys. 20, 12329–12345. https://doi.org/10.5194/acp-20-12329-2020.

Zhu, L., Jacob, D.J., Kim, P.S., Fisher, J.A., Yu, K., Travis, K.R., Mickley, L.J., Yantosca, R. M., Sulprizio, M.P., De Smedt, I., González Abad, G., Chance, K., Li, C., Ferrare, R., Fried, A., Hair, J.W., Hanisco, T.F., Richter, D., Jo Scarino, A., Walega, J., Weibring, P., Wolfe, G.M., 2016. Observing atmospheric formaldehyde (HCHO) from space: validation and intercomparison of six retrievals from four satellites (OMI, GOME2A, GOME2B, OMPS) with SEAC4RS aircraft observations over the southeast US. Atmos. Chem. Phys. 16, 13477–13490. https://doi.org/10.5194/acp-16-13477-2016.

Zoogman, P., Liu, X., Suleiman, R.M., Pennington, W.F., Flittner, D.E., Al-Saadi, J.A., Hilton, B.B., Nicks, D.K., Newchurch, M.J., Carr, J.L., Janz, S.J., Andraschko, M.R., Arola, A., Baker, B.D., Canova, B.P., Chan Miller, C., Cohen, R.C., Davis, J.E., Dussault, M.E., Edwards, D.P., Fishman, J., Ghulam, A., Gonzàlez Abad, G., Grutter, M., Herman, J.R., Houck, J., Jacob, D.J., Joiner, J., Kerridge, B.J., Kim, J., Krotkov, N.A., Lamsal, L., Li, C., Lindfors, A., Martin, R.V., McElroy, C.T., McLinden, C., Natraj, V., Neil, D.O., Nowlan, C.R., Osullivan, E.J., Palmer, P.I., Pierce, R.B., Pippin, M.R., Saiz-Lopez, A., Spurr, R.J.D., Szykman, J.J., Torres, O., Veefkind, J.P., Veihelmann, B., Wang, H., Wang, J., Chance, K., 2017. Tropospheric emissions: monitoring of pollution (TEMPO). J. Quant. Spectrosc. Ra. 186, 17–39. https://doi.org/10.1016/j.jqsrt.2016.05.008.